Metabolic heterogeneity of colorectal cancer as a prognostic factor: insights gained from fluorescence lifetime imaging

Anastasia D Komarova[1,2†], Snezhana D Sinyushkina[1†], Ilia D Shchechkin[1,2†], Irina N Druzhkova[1], Sofia A Smirnova[1], Vitaliy M Terekhov[3], Artem M Mozherov[1], Nadezhda I Ignatova[1], Elena E Nikonova[4], Evgeny A Shirshin[4,5], Liubov E Shimolina[1], Sergey V Gamayunov[3], Vladislav I Shcheslavskiy[1,6], and Marina V Shirmanova[1*]

[1]Institute of Experimental Oncology and Biomedical Technologies, Privolzhsky Research Medical University, Nizhny Novgorod, Russia; [2]Institute of Biology and Biomedicine, Lobachevsky State University of Nizhny Novgorod, Nizhny Novgorod, Russia; [3]Nizhny Novgorod Regional Oncologic Hospital, Nizhny Novgorod, Russia; [4]Laboratory of Clinical Biophotonics, Sechenov First Moscow State Medical University, Moscow, Russia; [5]Faculty of Physics, Lomonosov Moscow State University, Moscow, Russia; [6]Becker&Hickl GmbH, Germany

*For correspondence: Shirmanovam@gmail.com

[†]These authors contributed equally to this work

Competing interest: The authors declare that no competing interests exist

Abstract

Heterogeneity of tumor metabolism is an important, but still poorly understood aspect of tumor biology. Present work is focused on the visualization and quantification of cellular metabolic heterogeneity of colorectal cancer using fluorescence lifetime imaging (FLIM) of redox cofactor NAD(P)H. FLIM-microscopy of NAD(P)H was performed in vitro in four cancer cell lines, in vivo in the four types of tumors in mice and ex vivo in patients' tumor samples. The dispersion and bimodality of the decay parameters were evaluated to quantify the intercellular metabolic heterogeneity. Our results demonstrate that patients' tumors have significantly higher heterogeneity of energy metabolism compared with cultured cells and tumor xenografts, which was displayed as a wider and frequently bimodal distribution of a contribution of a free (glycolytic) fraction of NAD(P)H within a sample. Among patients' tumors, the dispersion was larger in the high-grade and early stage ones, without, however, any association with bimodality. These results indicate that cell-level metabolic heterogeneity assessed from NAD(P)H FLIM has a potential to become a clinical prognostic factor.

Key words: fluorescence lifetime imaging, FLIM, colorectal adenocarcinoma, tumor metabolism, metabolic heterogeneity, NAD(P)H, autofluorescence

Introduction

Reprogramming of energy metabolism is an established hallmark of malignant tumors. Tumor cells adjust their metabolism to sustain uncontrolled proliferation and tumor progression, even in the conditions of low nutrient supply and hypoxia. There are two main metabolic pathways for energy production in the form of ATP – glycolysis and oxidative phosphorylation (OXPHOS). For a long time, enhanced glycolysis has been considered as a central feature of tumor metabolism (DeBerardinis and Chandel, 2016). Unlike most normal cells, tumor cells rely on glycolysis not only in hypoxia (anaerobic glycolysis), but also in normoxia (aerobic glycolysis, or the Warburg effect), which provides them with many metabolic intermediates and a high-speed production of ATP for fast growth. The glycolytic shift in the tumors traditionally correlates with negative prognosis (Zhou et al., 2022). At the same time, mitochondrial OXPHOS is as important in malignant cells as glycolysis. Although defective mitochondria and lower OXPHOS capacity are often observed in cancer cells, this is not an absolute phenomenon – many tumors preserve functional mitochondria and normal OXPHOS rate (Gentric et al., 2017). Along with glucose, tumors use glutamine and fatty acids as alternative substrates. Interestingly, tumor cells are capable of switching between different metabolic pathways depending on their own needs and local environment, thus demonstrating a high degree of metabolic plasticity.

Therefore, tumor metabolism is currently viewed as a dynamic, variable system with a diversity of cellular metabolic states. In this context, intratumor heterogeneity means that there are the cells with different metabolic profiles in a tumor concurrently, and intertumor heterogeneity means that tumors of the same type and stage are characterized by the different metabolic strategies (Kim and DeBerardinis, 2019).

Heterogeneity of tumor metabolism can be caused by various factors (Shirmanova et al., 2023). Some of them («intrinsic») are related to tumor cells themselves: these are histogenesis of the tumor, mutation profile, (epi)genetics factors, differentiation state and proliferation activity, to name a few (Pavlova and Thompson, 2016; Sengupta and Pratx, 2016; Seth Nanda et al., 2020; Farhadi et al., 2022). Other reasons («extrinsic») are associated with the nonuniform microenvironment, e.g., local hypoxia, nutrient distribution, heterogeneity of the vasculature network, interaction of tumor cells with the extracellular matrix and stromal cells, etc. (Marusyk and Polyak, 2010; Masson and Ratcliffe, 2014; Yoshida, 2015; Stine et al., 2015). Collectively, these factors lead to variability of tumor metabolism in space and time. Metabolic heterogeneity as a part of general heterogeneity of tumors imposes some difficulties in patients' diagnosis and treatment and is believed to have a prognostic value (Liu, Wang et al., 2022; Liu, Xiang et al., 2022; Pinho, 2020).

Although metabolic heterogeneity is a well-recognized feature of tumors, its characterization at the cellular level remains scarce. In part, this is associated with the lack of the highly sensitive and direct techniques for its observation. Clinical imaging modalities, such as metabolic PET with radiolabeled tracers (^{18}F, ^{11}C) and MRI/MRS, allow to capture inter- and intratumor heterogeneity among patients with low (~4.5 mm) spatial resolution (Plathow and Weber, 2008). Recently evolved methods of single-cell sequencing deliver comprehensive information about the metabolic landscape of a tumor with a resolution up to 55–100 μm based on the expression of the metabolic genes, but these approaches are rather complex, laborious and not widely available (Evers et al., 2019; Huang et al., 2023).

Interrogation of cellular metabolism is possible with the laser scanning fluorescence microscopy that enables the detection of autofluorescence of the redox cofactors, such as the reduced form of the nicotinamide adenine dinucleotide (phosphate) – NAD(P)H and oxidized flavins (Georgakoudi and Quinn, 2023). Recording of the fluorescence decay parameters using the option of the fluorescence lifetime imaging (FLIM) allows the evaluation of the states of the cofactor molecules attributed to different metabolic pathways. The unbound state of NAD(P)H has a short lifetime (~0.4 ns), while the protein-bound state has a long lifetime (~1.7–3.0 ns) (Lakowicz et al., 1992). Changes in the relative fractions of the unbound and bound NAD(P)H in cancer cells calculated from biexponential fitting of decay curve typically indicate the shifts between glycolysis and OXPHOS (Rück et al., 2014). FLIM of NAD(P)H is currently considered as a promising, label-free technique for the assessment of metabolic heterogeneity of tumors at the (sub)cellular scale. Several studies, including ours, demonstrate the possibilities of NAD(P)H FLIM to visualize metabolic heterogeneity in cultured cells, multicellular structures in vitro, tumor xenografts in vivo and patients' tumors ex vivo (Shah et al., 2015; Skala et al., 2022; Lukina et al., 2019). However, quantifying the degree of tumor heterogeneity is lacking in most of these works.

In this paper, we present the results of assessment of cell-level metabolic heterogeneity of colorectal cancer using FLIM-microscopy of NAD(P)H. The distributions of the fluorescence decay parameters have been analyzed in the four colorectal cancer cell lines (HT29, HCT116, CaCo2, CT26), in the mouse tumor models in vivo generated from these cell lines and in the post-operative samples of patients' colon tumors. Quantification of heterogeneity has been performed with the dispersion and the bimodality index (BI) of the decay parameters. SHAP (SHapley Additive exPlanations) analysis has been conducted to find associations of the heterogeneity degree with clinical prognosis.

Results

1. Metabolic heterogeneity assessment in colorectal cancer cell lines

First, using FLIM of NAD(P)H, cellular metabolism was assessed in monolayer cultures of different colorectal cancer cell lines (Figure 1A). Typical values of NAD(P)H fluorescence lifetimes were registered for all cell lines – short τ_1 ~0.39 ns and long τ_2 ~2.30–2.90 ns (Table S1). Due to specifics of cellular metabolism, the relative contributions of the free (a_1) and bound (a_2) forms of NAD(P)H and, consequently, the mean lifetimes τ_m varied between the cell lines. The a_1 value decreased and τ_m increased in the following order: CT26 (~86%, 0.57 ns) > HCT116 (~84%, 0.71 ns) > HT29 (~80%, 0.80 ns) > CaCo2 (~73%, 0.94 ns) (Figure 1B, Table S1). A high NAD(P)H-a_1 (low τ_m) is an indicator of glycolytic shift, which is typical for cells with intense proliferation in a monolayer culture, like CT26 and HCT116. CaCo2 cells with the lowest a_1 value had more OXPHOS-shifted metabolism, which can be associated with the expression of morphological and functional characteristics of mature enterocytes of normal small intestine by this cell line (Lea, 2015). All cell lines statistically differ from each other (Table S4), and inter-cellular variations of the a_1 parameter were minor (<3%).

To quantify the metabolic heterogeneity, the BI was calculated for distributions of both a_1 (Figure 1C) and τ_m values (Figure S1). For all cell lines the BI of the a_1 distribution did not exceed 1.1 (the threshold of bimodality, Wang et al., 2009), justifying the uniformity of cell metabolism in a culture, which is consistent with the general view on standard cell lines as homogenous populations (Auman and McLeod, 2010; Idrisova et al., 2022). The BI-τ_m was, however, rather high (>1.0) in all cell lines except HCT116 (0.84). In the further experiments on tumors the BI-a_1 was used as more relevant.

Additionally, the dispersion of NAD(P)H-a_1 (D-a_1) was evaluated for each cell line to describe the extent of distribution of the data around the median (Table 1). The D-a_1 value varied from 1.67% in CT26 cell culture to 3.5% in CaCo2.

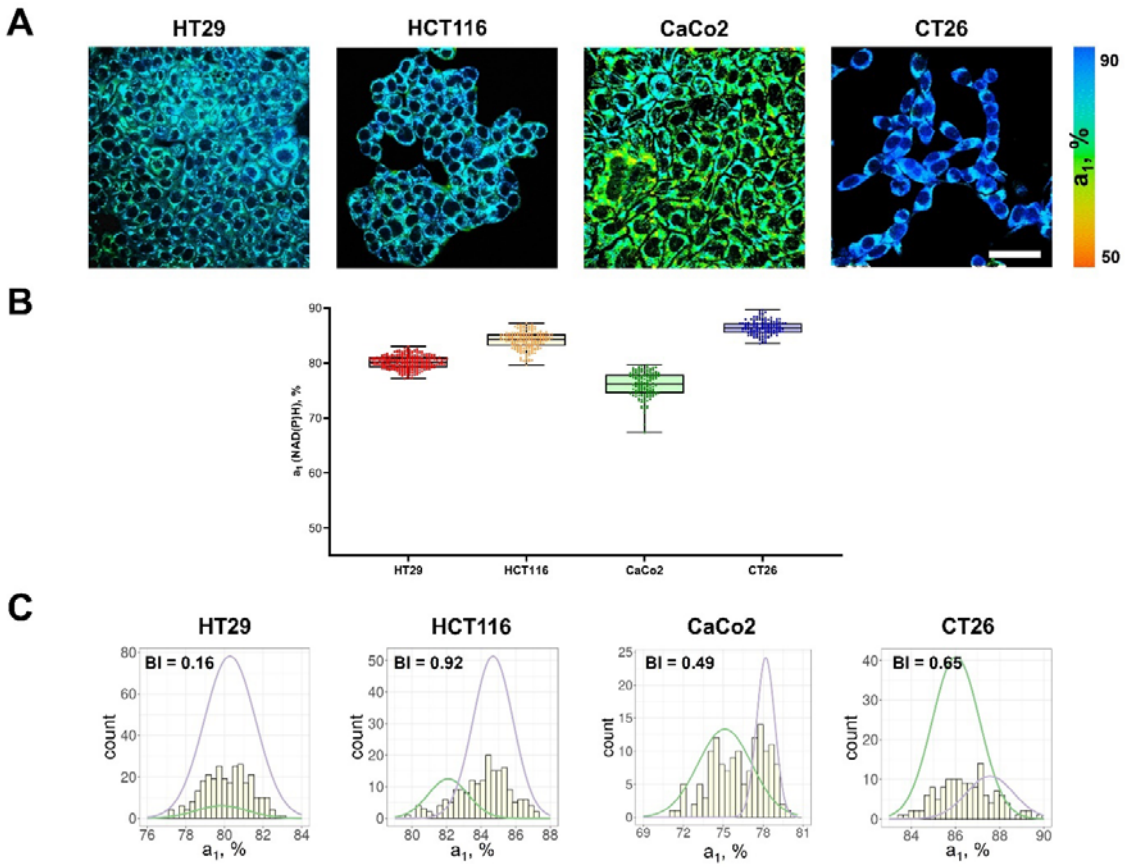

Figure 1. FLIM of NAD(P)H in monolayer cell cultures. (**A**) Representative FLIM images of colorectal cancer cell lines. Scale bar = 50 μm. For FLIM: ex. 750 nm, reg. 450–490 nm. (**B**) The relative contribution of free NAD(P)H (a_1, %) in cell cultures. Box shows the median and the quartiles Q1 and Q3, whiskers show minimum and maximum. Dots indicate individual cells (n=280 for HT29 cells, n=185 for HCT116 cells, n=146 for CaCo2 cells, n=138 for CT26 cells). p-values are shown in Table S4. (**C**) The distribution of the NAD(P)H-a_1 for the cell lines. The bimodality index (BI-a_1) is shown on each diagram.

2. Metabolic heterogeneity in mouse tumor models in vivo

Next, FLIM of NAD(P)H was performed in vivo on mouse tumor models, obtained from the colorectal cell lines shown above (Figure 2A). All the tumors were verified by histopathological analysis (Figure 2B).

Among the tumors, CT26 had the highest (~83%), and CaCo2 had, on average, the lowest (~76%, p-val=0.0028) contribution of free NAD(P)H a_1, similar to the cultured cells (Figure 2C, Table S1).

Most of the individual tumors showed larger (≥3%) inter-cellular variations of NAD(P)H-a_1 than corresponding cell lines, where the deviation from the median was ≤3%.

The dispersion D-a_1 was in the range of 2.6–4.02% (Table 1). At that, intertumor differences across each type of tumor were insignificant.

The BI-a_1 values in mouse tumors were generally higher than in monolayer cultures (Figure 2D, Table 1). In 4 of 12 tumors the BI-a_1 was ≥1.1, indicating the bimodal distribution of the a_1 parameter, i.e., the presence of two subpopulations of cells with different metabolism. Seven tumors had the BI-a_1 in the range of 0.7–1.0, which suggests that, while the distribution of the estimated parameter was unimodal, it was either wide or asymmetric, thus, also indicating some degree of heterogeneity. In 1 of 12 tumors the BI-a_1 was small (0.23), suggesting uniformity of cells' metabolism. Given the genetic identity of cells in standard cell lines, we can assume that the nonuniform microenvironment in the tumors was a major source of their variable metabolism.

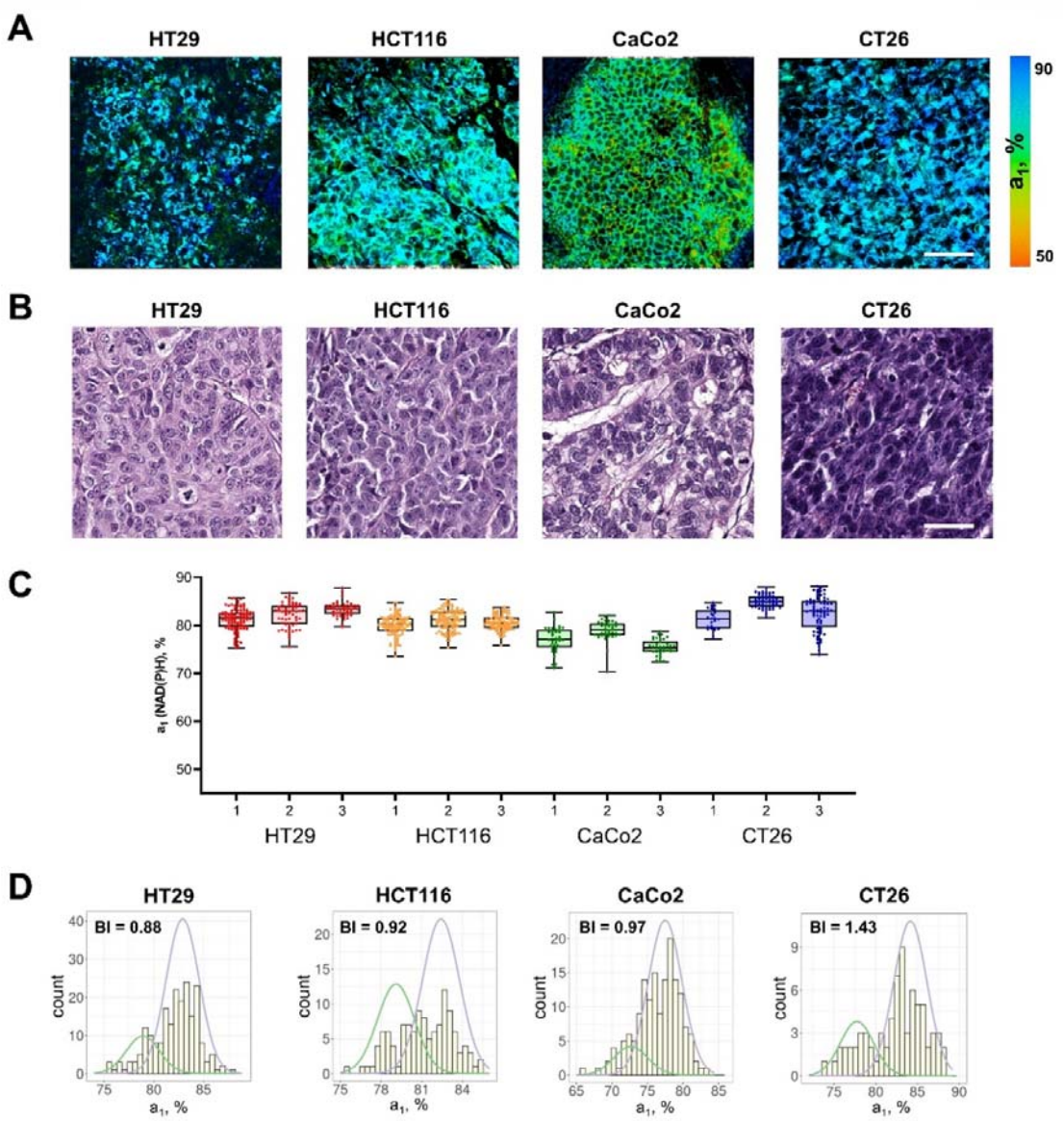

Figure 2. FLIM of NAD(P)H in mouse tumors in vivo. (**A**) FLIM images of NAD(P)H of tumor cells in mouse models in vivo. Scale bar = 50 μm. For FLIM: ex. 750 nm, reg. 450–490 nm. (**B**) Representative histological slices of tumors, hematoxylin/eosin (HE) staining, initial magnification 20×. Scale bar = 50 μm. (**C**) The relative contribution of free NAD(P)H (a_1, %) in tumors (numbered 1–3) obtained from different cell lines. Box shows the median and the quartiles Q1 and Q3, whiskers show minimum and maximum. Dots indicate individual cells (n=280 for HT29, n=340 for HCT116, n=160 for CaCo2, n=350 for CT26). p-values are shown in Table S4. (**D**) Representative distributions of the NAD(P)H-a_1 for each type of tumor. The bimodality index (BI-a_1) is shown on the diagrams.

3. Metabolic heterogeneity in colorectal cancer samples from patients

NAD(P)H FLIM images were collected from 29 postoperative samples of patients' colorectal adenocarcinomas, among which were the tumors of the I–IV stages, poorly and highly differentiated (Table 2). The representative FLIM and histological images are presented in Figure 3A and B correspondingly. Patients' tumors showed fluorescence lifetimes of τ_1 ~0.45 ns and τ_2 ~1.80–3.20 ns (Table S3), which were comparable with the values in human tumor xenografts (Table S1). The parameter NAD(P)H-a_1 was in the range of ~62–80% and NAD(P)H-τ_m was in the range of 0.80–1.20 ns, indicating that patients' tumors generally had larger variability of metabolic statuses than cancer cells in vitro and in xenografts in vivo.

A high degree of inter- and intratumor variability of cellular metabolism was detected in patients' tumors (Figure 3C). Less than half of the tumors (13 of 29) showed deviation of NAD(P)H-a_1 from the median <10% across the cells, and for the rest (16 of 29) the variations were 10–25%. The dispersion D-a_1 varied significantly among the samples, from 2.19% to 11.99%.

According to the heterogeneity assessment using the bimodality index, 14 of 29 tumors were metabolically highly heterogeneous (BI-a_1≥1.1) (Figure 3D, Table 1). In 14 tumors the BI-a_1 value was in the range of 0.50–1.0, which indicated the presence of metabolically different cells but not clearly separated into two clusters. Only one tumor sample (p16) was metabolically homogeneous (BI-a_1=0.24).

Notably, the bimodality index showed no correlation with dispersion. That is, among the samples there were those with bimodal distribution, but small dispersion of NAD(P)H-a_1 in a cell population (e.g., samples № 12, 13, 21), and vice versa (e.g., samples № 3, 7, 8).

Table 1. The Bimodality Index BI-a_1 and Dispersity D-a_1 of NAD(P)H in cultured cells, mouse tumors and patients' tumor samples.

Cell lines in vitro				
	HT29	HCT116	CaCo2	CT26
BI-a_1	0.16	0.92	0.49	0.65
D-a_1	1.83	2.01	3.38	1.67
Tumors in vivo				
	HT29	HCT116	CaCo2	CT26
BI-a_1	0.85 ± 0.61	0.93 ± 0.23	0.88 ± 0.13	**1.11 ± 0.51**
D-a_1	3.20	2.60	4.00	4.02

Patients' tumors ex vivo										
Sample	1	2	3	4	5	6	7	8	9	10
BI-a_1	**1.25**	0.81	1.01	**1.16**	1.01	1.00	0.86	0.70	**1.28**	**1.25**
D-a_1	7.77	4.18	8.68	11.99	6.93	7.83	9.33	8.25	11.51	6.96
Sample	11	12	13	14	15	16	17	18	19	20
BI-a_1	0.59	**1.45**	**1.34**	1.05	0.89	0.24	**1.29**	**1.32**	0.80	0.94
D-a_1	4.5	2.37	4.94	2.19	4.16	3.34	6.10	5.41	2.23	5.19
Sample	21	22	23	24	25	26	27	28	29	
BI-a_1	**1.28**	0.98	**1.53**	**1.31**	0.88	**1.58**	**1.65**	0.5	**1.29**	
D-a_1	5.27	3.29	6.54	5.77	4.87	5.83	4.14	5.67	6.36	

Therefore, using NAD(P)H FLIM we have observed and quantified metabolic heterogeneity of patients' colorectal tumors. Unlike tumor xenografts obtained from the cell lines that are thought to be genetically stable and identical, patients' tumors are genetically diverse, which could also contribute to their metabolic heterogeneity, in addition to microenvironmental factors.

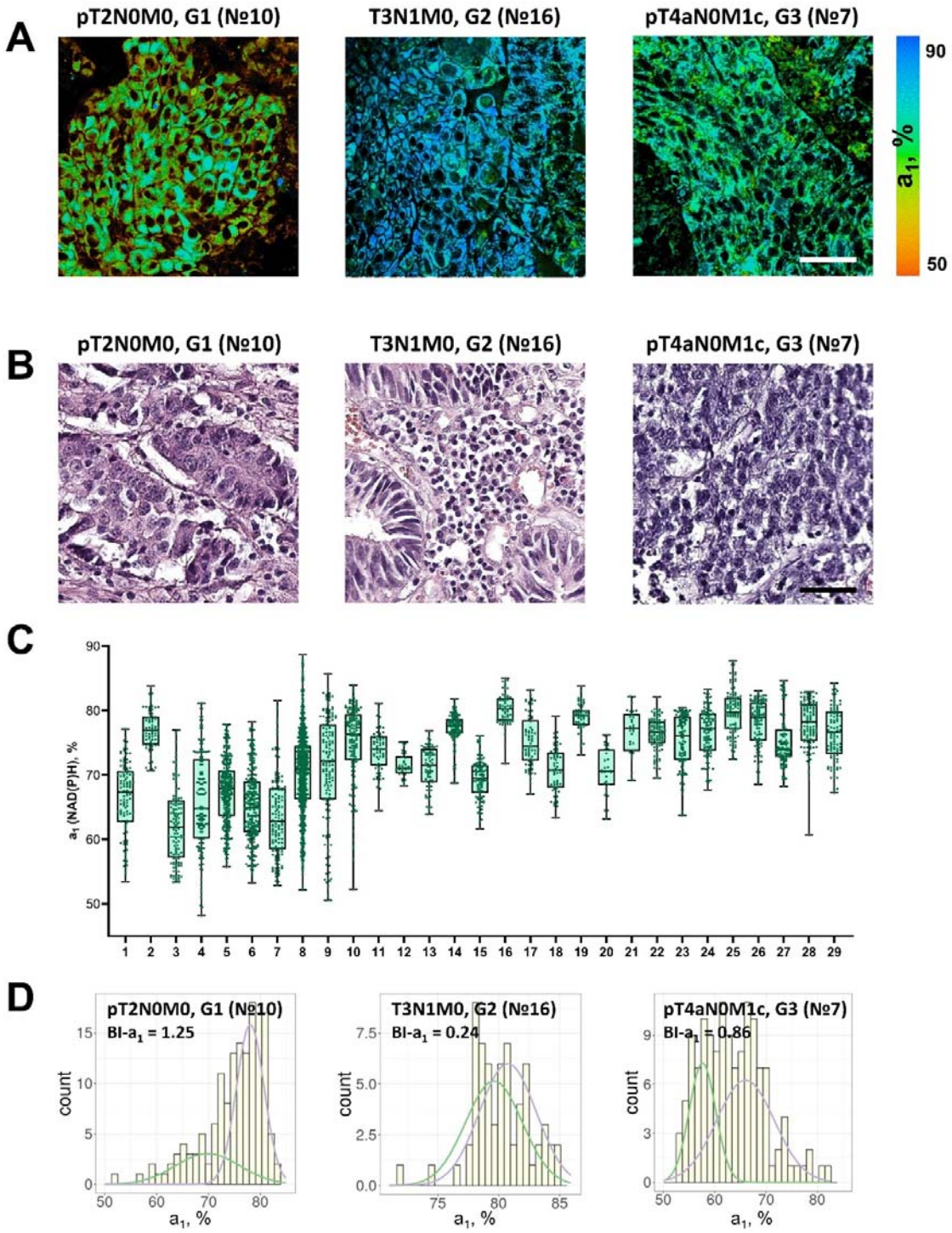

Figure 3. FLIM of NAD(P)H in patients' tumor samples ex vivo. (**A**) Representative FLIM images of patient tumors. Scale bar = 50 μm. For FLIM: ex. 750 nm, reg. 450–490 nm. (**B**) Histopathology of tumors, hematoxylin/eosin (HE) staining, initial magnification 20×. Scale bar = 50 μm. (**C**) The relative contribution of free NAD(P)H (a_1, %) in patients' tumors (numbered 1–29). Box shows the median and the quartiles Q1 and Q3, whiskers show

minimum and maximum. Dots are the measurements from the individual cells. (**D**) Representative distributions of the NAD(P)H-a_1 for patients' tumors. The bimodality index (BI-a_1) is shown on the diagrams.

Table 2. Information about patients and their colorectal tumors.

Characteristics	Number	Percent
Gender		
Male	16	55.17
Female	13	44.83
Age		
Mean ± SD	65.28±11.92 y.o.	-
Median	67 y.o.	-
Tumor staging		
I	3	10.34
IIA	6	20.69
IIB	3	10.34
IIIB	11	37.93
IIIC	1	3.45
IV	5	17.25
Tumor site		
Cecum colon	2	6.90
Transverse colon	10	34.48
Hepatic flexure	3	10.34
Sigmoid colon	8	27.59
Rectum	6	20.69
Grade		
Low (G1)	4	13.79
Moderate (G2)	19	65.52
High (G3)	6	20.69

4. Interrelation between metabolic heterogeneity and clinicopathological characteristics of tumors

The relationships between the metrics of cellular heterogeneity – the bimodality index BI and dispersion D of NAD(P)H fluorescence decay parameters – with the clinical parameters of the tumor, such as the stage according to the TNM system, and the grade (G),

were analyzed (Figure 4). Due to the small sample size, all tumors were divided into two groups by each parameter: T1+T2 and T3+T4; N0M0 and all the others with metastases; G1+G2 and G3.

SHAP analysis was used to estimate the importance of each variable (D-τ_2, D-a_1, D-τ_m, BI-τ_2, BI-a_1, BI-τ_m) coming from the biexponential decay curves for individual predictions. Fluctuations of τ_1 (fluorescence lifetime of free NAD(P)H) were not included in the analysis because they do not have a rational biological interpretation.

The results showed that, among the variables, dispersion of a_1 had a major relative weight in the prediction of all the clinical characteristics studied.

The tumors of the advanced stages T3 and T4 were characterized by reduced dispersion of a_1 compared with early stages T1 and T2, indicating their lower heterogeneity (Figure 4). The stage of the tumor T was significantly associated with the value of D-a_1 (p-val = 0.02).

If metastases were present (N and M were different from 0 in TNM), then those primary tumors showed a tendency to have lower D-a_1 compared with tumors for which metastases were absent (p-val = 0.056).

The high-grade tumors displayed a higher value of dispersion D-a_1 than the low-grade ones (Figure 4). Mann-Whitney U test showed a statistically significant difference between the groups of different grades (p-val = 0.04).

Other variables had no significant associations with clinicopathological parameters of the tumors and did not separate the groups of tumors reliably (see, for example, box-plots for BI-τ_m values, Figure S2).

Thus, the higher dispersion of free NAD(P)H fraction in a sample was characteristic of colorectal tumors of early stages (T1, T2) and high grade (G3) and thus showed a potential as a prognostic marker.

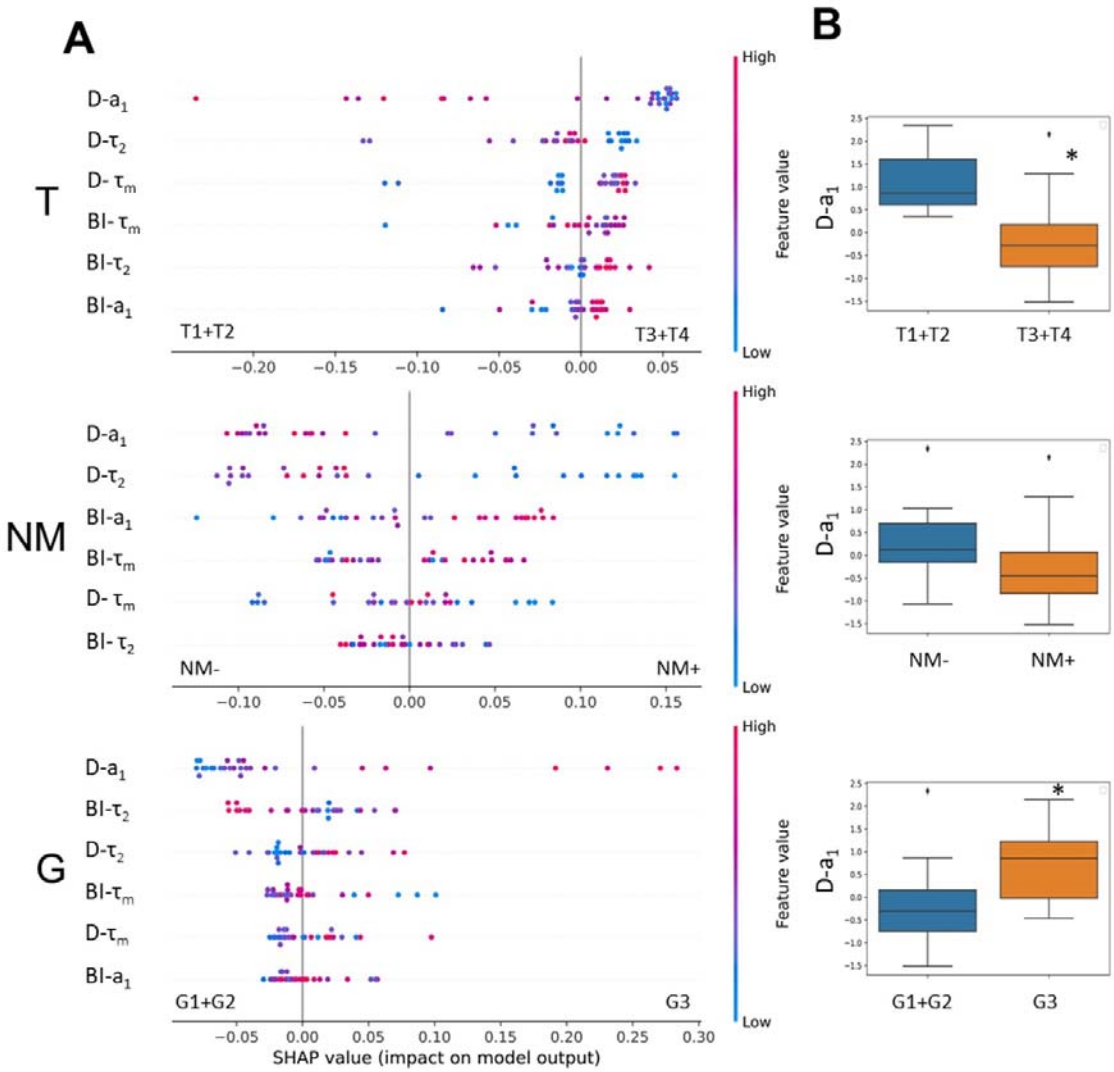

Figure 4. The relationships between metabolic heterogeneity and clinicopathological characteristics of patients' tumors. (**A**) Plots of SHAP analysis for the built decision tree models to determine the importance of dispersion (D) and bimodality index (BI) of the fluorescence decay parameters of NAD(P)H. The higher the value of the variable, the more red the dot is. (**B**) Box-plots of D-a_1 with highest significance, * p-val < 0.05.

Discussion

The altered energy metabolism is known to support tumor progression because tumor cells are critically in need of ATP for uncontrolled proliferation and growth. It has been established that tumor cells explore different metabolic programs and utilize multiple fuels even within one tumor, thus leading to metabolic heterogeneity. Until recently, direct observation of cell-level heterogeneity of tumor metabolism was a challenging task, but became possible with the evolution of advanced optical microscopic techniques, such as two-

photon fluorescence lifetime microscopy, FLIM. In the present research, using FLIM of redox cofactor NAD(P)H, which possesses endogenous fluorescence, we compared metabolic features of colorectal cancer cells across in vitro and in vivo models and patients' samples. For the first time, it was shown that heterogeneity of cellular metabolism increases with model complexity and is the highest at the level of patients' tumors. The heterogeneity was quantified on the basis of FLIM data and correlated with clinical characteristics of the tumors, which has not been done before.

A lot of studies, including the works of our group, demonstrate the possibilities of FLIM for assessment of the intra- and intertumor heterogeneity of metabolism in different models. Using NAD(P)H FLIM, metabolic heterogeneity was revealed in colorectal cancer cell cultures obtained from the patients' tumors, whereas the cells of the standard cell lines were uniform in their metabolism (Shirshin et al., 2022). J. Chacko and K. Eliceiri observed intercellular heterogeneity of metabolism in the MCF10A human breast epithelial cell line (Chacko and Eliceiri, 2019). Several studies show metabolic heterogeneity of 3D multicellular structures. For example, tumor spheroids obtained from the cervical cancer cell line HeLa (Lukina et al., 2018) or murine colorectal carcinoma cell line CT26 (Shirmanova et al., 2021) displayed the differences in metabolism between the outer and the inner cell layers with the outer layers being more glycolytic (higher NAD(P)H-a_1). The spheroids generated from the patients' derived glioblastoma cultures did not show metabolic zonality, but generally had greater intercellular variations of NAD(P)H lifetime parameters than the spheroids from standard line U373 MG (Yuzhakova et al., 2023). A spectrum of works by M. Skala' group demonstrates an opportunity of the optical metabolic imaging for heterogeneity assessment in patient tumor-derived organoids on the example of a breast, pancreatic (Sharick et al., 2020; Walsh et al., 2014; Walsh et al., 2017), head and neck (Shah et al., 2017), colorectal cancers (Skala et al., 2022).

In the research in vivo, the heterogeneous structure of tumor and its microenvironment was shown on PyMT mammary tumors (Burkel et al., 2022). Analysis of the optical metabolic parameters revealed heterogeneity of the B78 mouse melanoma model, caused by different microenvironments (Heaton et al., 2023). The authors suggested that tumor heterogeneity could be induced by such factors as pH, nutrient and oxygen availability, or activation of immune cells. In the in vivo study on HeLa tumor xenografts, metabolically different cells were detected in the cellular and collagen-rich areas (Shirmanova et al., 2018). Recently, we demonstrated a high variability of cellular metabolic statuses in CT26 tumors of large size compared with small tumors, which correlated with heterogeneous oxygen

distribution (Parshina et al., 2022). A significant intertumor heterogeneity of metabolism was observed in patient-derived glioblastoma xenografts, which differed them from standard U87 glioma (Yuzhakova et al., 2022).

In our study, we compared metabolic FLIM parameters of colorectal cell lines, mouse tumor models and patients' colorectal tumors. As expected, intercellular heterogeneity of metabolism was the highest in patients' tumor samples as followed from a wide and often bimodal distribution of NAD(P)H-a_1. This result is consistent with the study by J. Auman and H. McLeod using genome-wide gene expression data; the authors concluded that colorectal cancer cell lines lack the molecular heterogeneity of clinical colorectal tumors (Auman and McLeod, 2010).

Cell-level metabolic heterogeneity may be present in the cell population initially, as discussed above, or develop during the treatment. The heterogeneous metabolism after treatment was detected in tumor organoids (Walsh et al., 2016; Walsh et al., 2014; Gillette et al., 2021) and in animal models (Heaster et al., 2019). In any case, the presence of metabolically distinct cells led to the varying drug responses.

An assessment of metabolic heterogeneity in patients' tumors seems valuable from a clinical point of view. The great efforts to translate FLIM in the clinical setting both in vivo and ex vivo have been done by several groups (Jo et al., 2018; Alfonso-Garcia et al., 2023; Weyers et al., 2022; Seidenari et al., 2012; Mycek et al., 1998; Herrando et al., 2024; Lagarto et al., 2020). Clinical translation is spearheaded through macroscopic implementation and point-spectroscopy approaches that are capable of large sampling areas and enable access to otherwise constrained spaces but lack cellular resolution, making the interpretation of the results a complicated task. Previously, using NAD(P)H FLIM-microscopy of postoperative samples, we observed a high degree of inter- and intratumor heterogeneity of T3 stage colorectal tumors in comparison with normal colon samples (Lukina et al., 2019). Unfortunately, most of the tumor types are inaccessible for microscopic investigation in patients using clinically approved techniques. The exception is the skin tumors that can be inspected with clinical systems, like MPTflex or MPTcompact (JenLab, Germany). At the same time, endoscopic FLIM-microscopy has been developing actively since the last ten years, which opens the prospects for in vivo examination of a wide spectrum of patients' tumor types (Sun et al., 2013; Farhadi et al., 2022). In principle, an assessment of tumor metabolism in biopsy samples is also possible, which widens the potential clinical applications of FLIM.

Although metabolic heterogeneity at the cellular level has been reported for different models and patient-derived cells, the comparisons between different samples and studies are hard to make as most of them lack any quantification of the heterogeneity.

Different approaches have been proposed to quantify the metabolic differences identified by FLIM. For example, in the papers (Shah et al., 2015; Sharick et al., 2019) a heterogeneity index and its modified form the weighted heterogeneity index (wH-index) were used for quantitative analysis of cellular heterogeneity. The wH-index is based on the Gaussian distribution models and is a modified form of the Shannon diversity index. Using this index the authors described the variations of a combination of parameters, such as NAD(P)H fluorescence lifetime, FAD fluorescence lifetime and optical redox ratio, defined as the OMI-index. The methods developed in Ref. (Heaster et al., 2019) established the combination of optical metabolic imaging variables and spatial statistical analysis (spatial proximity analysis, spatial clustering, multivariate spatial analysis, spatial principal components analysis) to quantify the spatial heterogeneity of tumor cell metabolism. Recently, we have proposed a new quantitative criterion – the bimodality index (BI) – to accurately discriminate between metabolically diverse cellular subpopulations on the basis of NAD(P)H FLIM data (Shirshin et al., 2022). The BI provides dimensionless estimation on the inherent heterogeneity of a sample by checking the hypothesis about approximation of a fluorescence decay parameter distribution by two Gaussians. Using the BI, the metabolic heterogeneity has been identified in standard and primary cancer cells cultures after chemotherapy with 5-fluorouracil.

Here, we used the dispersion of NAD(P)H D-a_1 and bimodality index BI-a_1 for quantifying metabolic heterogeneity of patient's tumors and compared it with in vitro and in vivo models. Of these two metrics of heterogeneity, the dispersion appeared more valuable in terms of tumor prognosis. Our results on patients' colorectal tumors revealed some associations between the dispersion of a_1 within a sample and tumor stage – the early-stage tumors (T1, T2) were metabolically more heterogeneous than the late-stage ones (T3, T4). A degree of heterogeneity was also associated with differentiation state, a stage-independent prognostic factor in colorectal cancer where the lower grade correlates with better the prognosis. The high-grade (G3) tumors had significantly higher dispersion of a_1, compared with low-grade ones (G1, G2). These results have a rational explanation from the point of view of biological significance of heterogeneity. In stressful and unfavorable conditions, to which the tumor cells are exposed, the spread of the parameter distribution in the population rather than the presence of several distinct clusters (modes) matters for adaptation and

survival. The high diversity of cellular metabolic phenotypes provided the survival advantage, and so was observed in more aggressive (undifferentiated or poorly differentiated) and the least advanced tumors.

One of the possible reasons for metabolic heterogeneity could be the presence of stromal cells or diversity of epithelial and mesenchymal phenotypes of cancer cells within a tumor. Immunohistochemical staining of tumors for EpCam (epithelial marker) and vimentin (mesenchymal marker) showed that the fraction of epithelial, EpCam-positive, cells was more than 90% in tumor xenografts and on average 76±10 % in patients' tumors (Figure S3). However, the ratio of EpCam- to vimentin-positive cells in patients' samples neither correlated with D-a_1 nor with BI-a_1, which means that the presence of cells with mesenchymal phenotype did not contribute to metabolic heterogeneity of tumors identified by NAD(P)H FLIM.

Metabolic heterogeneity of colorectal cancer is discussed in the literature. The focus of many of these studies is on the molecular classification of tumors by the analysis of their metabolic features. For example, Zhang et al. showed that colorectal tumors could be classified into three distinct metabolism-relevant subtypes and developed a metabolism-related signature consisting of 27 metabolic genes, which were expressed differentially among the three subtypes and correlated with patients' overall survival (Zhang et al., 2020). Varshavi et al. performed metabolic characterization of colorectal cancer cells depending on KRAS mutation status using ^{1}H NMR spectra of the metabolites. They revealed that some mutations led to an increase of glucose consumption and lactate release, while others, on the contrary, decreased it (Varshavi et al., 2020). Numerous studies have investigated the prognostic potential of key metabolic (mainly glycolytic) enzymes assessed from immunohistochemistry (IHC). For example, glucose transporter 3 (GLUT3) was highly expressed in colorectal cancer tissues of 63% of patients as relative to benign tissues and correlated with poor clinical outcomes (Dai et al., 2020). In the study by Offermans et al. a sum score based on the expression levels of six proteins (PTEN, p53, GLUT1, PKM2, LDHA, MCT4) in colorectal cancer showed worse survival of patients with a higher probability of the Warburg effect (Offermans et al., 2022). Mizuno et al. found that expression of lactate dehydrogenase A (LDHA) at the invasive margin of the tumor was weaker than in the center (Mizuno et al., 2020). Note that standard molecular genetics and immunolabeling techniques identify the metabolic differences between tumors or between large areas within a tumor, while a single cell level metabolic information is lacking. We

have verified the inability of IHC to detect intercellular differences in metabolic states based on the expression of LDHA and GLUT3 (Fig. S4).

Liu et al. found a correlation between intratumor metabolic heterogeneity parameters of ^{18}F-FDG PET/CT and KRAS mutation status in colorectal cancer – KRAS mutant tumors had more ^{18}F-FDG uptake and heterogeneity than wild-type KRAS (Liu, Wang et al., 2022). In a different study they showed that intratumor metabolic heterogeneity assessed from ^{18}F-FDG PET/CT is an important prognostic factor for progression-free survival and overall survival in patients with colorectal cancer (Liu, Xiang et al., 2022). The value of intratumoral metabolic heterogeneity in ^{18}F-FDG PET/CT for prediction of recurrence in patients with locally advanced colorectal cancer was also demonstrated by Han et al. (Han et al., 2018). In the study by Zhang et al. intratumoral metabolic heterogeneity derived from ^{18}F-FDG PET/CT was higher in colorectal tumors with a high microsatellite instability (MSI) – an important prognostic biomarker, and predicted MSI in stage I–III colorectal cancer patients preoperatively (Zhang et al., 2023). Lin et al. identified two subtypes of colorectal cancer using a metabolic risk score based on genes that were mostly involved in lipid metabolism pathways; this criterion was applied for survival prediction – patients with a higher metabolic risk score had worse prognosis (Lin et al., 2021). Therefore, these clinical studies consider intratumor metabolic heterogeneity as a useful prognostic factor.

In the context of metabolic heterogeneity assay using NAD(P)H FLIM, some limitations should be mentioned. If the investigation of patients' tumor metabolism is performed on ex vivo tissue samples, one should be careful to work with freshly excised tissue or store the sample in the appropriate conditions. As we found previously, FLIM parameters of autofluorescence change very quickly (within 15 min) on air, but can be preserved in 10% BSA on ice during 3 h (Lukina et al., 2019). A limitation of our study is that microscopic FLIM images of the tissues were processed manually to obtain information about each individual cell, which made the analysis time-consuming. The methods for segmentation of tissue images have been continuously developed in digital histopathology (Ahmed et al., 2022; van der Laak et al., 2020). As for FLIM, there are approaches to automatic segmentation of FLIM images of cell cultures and some normal tissues on the basis of machine learning (Smith et al., 2019). So, in spite of the complex and heterogeneous tissue architecture, there are expectations that the task of identification of the individual cells in FLIM images of tumor tissues will be solved in the nearest future. Finally, a small size of the microscopic field of view (typically less 300 μm) limits the inspected area within the tumor

sample. Taking into account a high spatial heterogeneity of clinical tumors, there is no confidence whether the inspected area is sufficiently representative.

Fluorescence of flavins can also serve as a biomarker of cellular metabolism independently of or in conjunction with NAD(P)H, for example in the optical redox ratio, OMI or FLIRR indexes (Walsh et al., 2014; Wallrabe et al., 2018; Kalinina et al., 2021). With the aim to assess metabolic heterogeneity in colorectal cancer, we have made an attempt to record the signal from flavins in addition to NAD(P)H (Fig. S5). However, its intensity was very low (~27 times lower than NAD(P)H) and insufficient to collect the required number of photons for correct fitting. Yet, this observation does not exclude that flavins can be useful in the heterogeneity assays of cancer of different origin.

Owing to the high (sub)cellular resolution (~200–500 nm), FLIM-microscopy provides unique information about metabolic heterogeneity, unavailable with any other methods, like ^{18}F-FDG PET/CT, spatial transcriptomics or immunohistochemistry. Therefore, FLIM-microscopy of endogenous cofactors is not only a powerful research technique, which is capable of improving our understanding of cellular metabolic diversity, but also the tool with a great potential for clinical translation to predict disease outcome.

Conclusions

It is now evident that metabolic processes in cancer are highly variable, which make the tumor metabolism extremely heterogeneous. Metabolic heterogeneity of tumors complicates treatment efforts and is thought to be a negative prognostic factor. Due to the lack of methods for direct observation and quantification of metabolic heterogeneity at cellular level, it has been poorly characterized so far. Our assessments of cell-level heterogeneity from FLIM-microscopy of NAD(P)H clearly show that heterogeneous metabolic landscape of a patient' tumor is hardly reproducible in in vitro and in vivo models, which underlie the importance of such investigations on clinical material. Although the present research included a limited number of patients (n=29), the obtained results showing the associations between metabolic heterogeneity and clinical features of tumors allow us to consider it as a potential prognostic marker. We plan to continue this study to collect more tumor samples and estimate the correlations between their metabolic heterogeneity and follow-up clinical outcomes.

Materials and methods

Cell Cultures. The human colorectal carcinoma cell lines HT29, HCT116, CaCo2 and murine colon carcinoma cell line CT26 were used in the study. Cells were grown in Dulbecco's modified Eagle's medium (DMEM) (Gibco, Carlsbad, CA, USA) supplemented

with 10% fetal bovine serum (FBS) (Gibco, Carlsbad, CA, USA), 2 mM glutamine (Gibco, Carlsbad, CA, USA), 10 mg/mL penicillin (Gibco, Carlsbad, CA, USA), 10 mg/mL streptomycin (Gibco, Carlsbad, CA, USA). The cells were incubated at 37°C, 5% CO_2, and 80% relative humidity and passaged three times a week. The passaging of cells was carried out at a confluence of 70–80% with trypsin-EDTA (Thermo Fisher Scientific, Waltham, MA, USA).

For fluorescence microscopic studies the cells were seeded in 35 mm glass-bottomed FluoroDishes (Ibidi GmbH, Gräfelfing, Germany) in the amount of $5x10^5$ cells in 2 mL of DMEM and incubated for 24 h (37°C, 5% CO_2). Before FLIM, DMEM was replaced with the FluoroBrite DMEM (Thermo Fisher Scientific, Waltham, MA, USA) for fluorescence imaging.

Cell culture experiments included two independent replicates for each cell line, the data from which were then combined.

Tumor Models. In vivo experiments were performed on female nude and Balb/C mice weighing ~20–22 g. All animal protocols were approved by the Local Ethical Committee of the Privolzhsky Research Medical University (Nizhny Novgorod, Russia). To generate tumors, the suspensions of cancer cells were injected subcutaneously into the tight in the following amount: 1.5×10^6 of HT29 cells in 100 µL PBS, 1.0×10^6 of HCT116 cells in 100 µL PBS, 5.5×10^6 of CaCo2 cells in 100 µL PBS. CT26 cells (2.0×10^5 cells in 20 µL PBS) were inoculated intracutaneously in the ear. The tumor volume was measured using a caliper, and calculated using the formula v=a×b×1/2b, where a is the length and b is the width of the tumor. In vivo studies were done on 21st day of growth for HT29 tumors (244.8±36.6 mm^3), on the day 23 for HCT116 (533.9±42.0 mm^3), on the day 68 for CaCo2 (397.8±65.2 mm^3), and on the day 14 for CT26 (60.9±5.6 mm^3). The groups of mice with each tumor type included 3 animals.

Mice were anesthetized by an intramuscular injection of Zoletil (40 mg/kg, Virbac SA, France) and 2% Rometar (10 mg/kg, Spofa, Czech Republic) for intravital microscopy. The skin over the tumor was opened and covered with a coverslip.

Patient samples. Twenty-nine surgical samples of patients' colorectal tumors were obtained in the Nizhny Novgorod Regional Oncological Center (Nizhny Novgorod, Russia) during the tumor resection. The study with the use of patients' material was approved by the ethics committee of the Privolzhsky Research Medical University (approval № 09 from 30.06.2023). All the patients gave informed written consent prior to the enrollment in the study.

All the patients had a histological verification of colorectal adenocarcinoma, the stage definition according to the TNM system, and the definition of the grade. There were tumors of the I–IV stage of low (G1), moderate (G2) and high (G3) grade. The tumors were localized in different sites of the large intestine (caecum, colon, rectum). 27 of 29 patients did not receive any anti-cancer therapy before the surgery, 2 patients (7 and 8) have been pretreated with radiotherapy or chemotherapy. The detailed information about patients' tumors is presented in Table 2, data about their clinicopathological characteristics is presented in Table S2.

Immediately after surgical excision, tumor samples, 0.5–1 cm^3 in size, were wrapped in gauze soaked in a solution of 10% BSA (bovine serum albumin), placed in sterile Petri dish on ice, transferred to the laboratory within 30 min and examined on the laser scanning microscope immediately. This storage protocol allows to preserve autofluorescence lifetime parameters unchanged for at least 3 hours (Lukina et al., 2019).

FLIM-microscopy. FLIM of NAD(P)H was performed using the laser scanning microscope LSM 880 (Carl Zeiss, Germany) equipped with a TCSPC-based FLIM module (Becker & Hickl GmbH, Germany). The Ti:Sa femtosecond laser MaiTai HP (Spectra-Physics Inc., USA, repetition rate 80 MHz, pulse duration 120 fs) was used for two-photon excitation of NAD(P)H at a wavelength of 750 nm. Fluorescence signal was registered in the range 450–490 nm. The laser power applied to the samples was ~6 mW. FLIM images were obtained using the water-immersion objective C-Apochromat W Korr 40×/1.3 (Carl Zeiss, Germany). Image collection time was 60 s. In total, 5–10 images were obtained from each sample.

FLIM images were processed in the SPCImage 8.5 software (Becker & Hickl GmbH, Germany). NAD(P)H fluorescence was analyzed in the cytoplasm of individual cells, in total 50–200 cells in each sample. Fluorescence decay curves were fitted by a bi-exponential model with a goodness of fit χ^2 0.8–1.2. The following fluorescence decay parameters were analyzed: short component corresponding to the free form of NAD(P)H (τ_1), long component corresponding to the protein-bound NAD(P)H (τ_2), their relative contributions (a_1 и a_2, correspondingly, $a_1+a_2=100\%$), and the mean fluorescence lifetime ($\tau_m = \frac{a_1 \times \tau_1 + a_2 \times \tau_2}{a_1 + a_2}$).

Histopathology and Immunohistochemistry (IHC). Formalin-fixed tumor samples were embedded in paraffin according to standard procedure and cut parallel to the optical plane. The sequential sections 7 μm thick were stained with hematoxylin and eosin, sections 4 μm thick were used for immunohistochemical staining.

Tissue sections were imaged using EVOS M7000 Imaging System (Thermo Fisher Scientific Inc., Waltham, MA USA).

Statistical Analysis. The obtained data were checked for the normal distribution using the Kolmogorov–Smirnov's criterion. The data with a normal distribution were presented as mean ± standard deviation (SD). The data with an abnormal distribution were presented as a median and 25% and 75% quantiles (Q1 and Q3). The ANOVA test for comparison data with a normal distribution and the Kruskal-Wallis's test for comparison data with an abnormal distribution were used, with p-val<0.05 being considered statistically significant. Statistical data processing was performed in IBM SPSS Statistics 26.0, R-studio, Python.

Bimodality Index and Dispersion calculation. A continuous measure known as the «bimodality index» is utilized to gauge the degree of conformity of a set of univariate data to a two-component mixture model. The score is larger if the two components are balanced in size or if the separation between the two modes is larger. The BI≥1.1 is considered as a cutoff to reliably define a bimodal distribution in the data (Wang et al., 2009; Shirshin et al., 2022).

BI was calculated according to the equation:

$$BI = \delta \times \sqrt{p(1-p)}, \delta = \frac{|\mu_1 - \mu_2|}{\sqrt{\sigma_1 \sigma_2}}, p = \frac{n_1}{n_1 + n_2},$$

where μ – the mean of each Gaussian, σ – the standard deviation of each Gaussian and n – the number of measurements of each Gaussian.

Dispersion was calculated as interquartile range: 75% quantile – 25% quantile (Q3 – Q1).

The parameters τ_m and a_1 obtained by FLIM microscopy were used to calculate the bimodality indices (BI) and the dispersion for cultured cells, mouse tumors and patients' samples.

The resulting BI for τ_m and a_1 and dispersion of a_1 were used to search for the relationships between them and the pathophysiological parameters of tumors: the TNM stage and the grade (G).

The fluorescence decay parameters were normalized using the z-normalization method to level out the numerical difference.

A random forest decision tree model was used to evaluate the importance of fluorescence decay parameters for clinicopathological characteristics. The model was used for feature selection analysis, by which the most significant ones are selected among the variables that define the sample. The random forest method delimited the variable space by

attempting to reduce the Gini index as much as possible and partition the space into blocks containing only one type of sample. The model results were used for SHAP (SHapley Additive ExPlanations) analysis, which is designed to evaluate each variable for its ability to delimit space. SHAP analysis identified the most significant parameters, which were studied by classical statistical method (Mann-Whitney).

SHAP analysis is a technique used to explain the output of any machine learning model. SHAP analysis displays the relative influence of variables (decay parameters derivatives) on a model's output and can provide insight into the most significant factors and the impact of variables on the outcome. SHAP values are a way to explain the contribution of each object to the model output. They measure how much each variable contributes to the model’s prediction and can help determine which variables are most important to the model and how they affect the outcome.

The T parameter from TNM was modified in a way that classes 1+2 became group 0, and 3+4 became group 1. The modification of the parameter G resulted in two classes: classes 1+2 became group 0 and class 3 became group 1. Parameters N and M were modified as NM, in which the class was distinguished: no metastases – 0, metastases – 1. Since the clinical parameters, in a modified form, are binary, a point-biserial correlation coefficient was chosen to assess the correlation.

Acknowledgements

The authors are grateful to Dr. Anton Plekhanov (PRMU) and Dr. Maria Lukina for helpful discussions and valuable suggestions and to Daria Myalik (PRMU) and Artem Grishin (PRMU) for their help with immunohistochemistry.

Funding

This work was supported by the Russian Science Foundation (Project No. 23-15-00294).

Competing interests

The authors declare no conflict of interest.

References

Ahmed AA, Abouzid M, Kaczmarek E. 2022. Deep Learning Approaches in Histopathology. *Cancers (Basel)* **14**:5264. doi: 10.3390/cancers14215264.

Alfonso-Garcia A, Anbunesan S, Bec J, Lee H, Jin L, Bloch O, Marcu L. 2023. In vivo characterization of the human glioblastoma infiltrative edge with label-free intraoperative fluorescence lifetime imaging. *Biomed Opt Express* **14**:2196–2208. doi: 10.1364/BOE.481304.

Auman JT, McLeod HL. 2010. Colorectal Cancer Cell Lines Lack the Molecular Heterogeneity of Clinical Colorectal Tumors. *Clinical Colorectal Cancer* **9**:40–47. doi:10.3816/CCC.2010.n.005

Burkel BM, Inman DR, Virumbrales-Muñoz M, Hoffmann EJ, Ponik SM. 2022. A Label-Free Segmentation Approach for Intravital Imaging of Mammary Tumor Microenvironment. *JoVE* 63413. doi:10.3791/63413

Chacko JV, Eliceiri KW. 2019. Autofluorescence lifetime imaging of cellular metabolism: Sensitivity toward cell density, pH, intracellular, and intercellular heterogeneity. *Cytometry Pt A* **95**:56–69. doi:10.1002/cyto.a.23603

Dai W, Xu Y, Mo S, Li Q, Yu J, Wang R, Ma Y, Ni Y, Xiang W, Han L, Zhang L, Cai S, Qin J, Chen WL, Jia W, Cai G. 2020. GLUT3 induced by AMPK/CREB1 axis is key for withstanding energy stress and augments the efficacy of current colorectal cancer therapies. *Signal Transduct Target Ther* **5**:177. doi: 10.1038/s41392-020-00220-9.

DeBerardinis RJ, Chandel NS. 2016. Fundamentals of cancer metabolism. *Sci Adv* **2**:e1600200. doi:10.1126/sciadv.1600200

Evers TMJ, Hochane M, Tans SJ, Heeren RMA, Semrau S, Nemes P, Mashaghi A. 2019. Deciphering Metabolic Heterogeneity by Single-Cell Analysis. *Anal Chem* **91**:13314–13323. doi:10.1021/acs.analchem.9b02410

Farhadi P, Yarani R, Valipour E, Kiani S, Hoseinkhani Z, Mansouri K. 2022. Cell line-directed breast cancer research based on glucose metabolism status. *Biomedicine & Pharmacotherapy* **146**:112526. doi:10.1016/j.biopha.2021.112526

Gentric G, Mieulet V, Mechta-Grigoriou F. 2017. Heterogeneity in Cancer Metabolism: New Concepts in an Old Field. *Antioxidants & Redox Signaling* **26**:462–485. doi:10.1089/ars.2016.6750

Georgakoudi I, Quinn KP. 2023. Label-Free Optical Metabolic Imaging in Cells and Tissues. *Annu Rev Biomed Eng* **25**:413–443. doi:10.1146/annurev-bioeng-071516-044730

Gillette AA, Babiarz CP, VanDommelen AR, Pasch CA, Clipson L, Matkowskyj KA, Deming DA, Skala MC. 2021. Autofluorescence Imaging of Treatment Response in Neuroendocrine Tumor Organoids. *Cancers* **13**:1873. doi:10.3390/cancers13081873

Han Y-H, Jeong H-J, Sohn M-H, Lim ST. 2018. Clinical value of intratumoral metabolic heterogeneity in [18F]FDG PET/CT for prediction of recurrence in patients with locally advanced colorectal cancer. *Q J Nucl Med Mol Imaging* **62**. doi:10.23736/S1824-4785.16.02862-4

Heaster TM, Landman BA, Skala MC. 2019. Quantitative Spatial Analysis of Metabolic Heterogeneity Across in vivo and in vitro Tumor Models. *Front Oncol* **9**:1144. doi:10.3389/fonc.2019.01144

Heaton AR, Rehani PR, Hoefges A, Lopez AF, Erbe AK, Sondel PM, Skala MC. 2023. Single cell metabolic imaging of tumor and immune cells in vivo in melanoma bearing mice. *Front Oncol* **13**:1110503. doi:10.3389/fonc.2023.1110503

Herrando AI, Castillo-Martin M, Galzerano A, Fernández L, Vieira P, Azevedo J, Parvaiz A, Cicchi R, Shcheslavskiy VI, Silva PG, Lagarto JL. 2024. Dual excitation spectral autofluorescence lifetime and reflectance imaging for fast macroscopic characterization of tissues. *Biomedical Optics Express* **15**: 3507–3522. doi:10.1364/BOE.505220.

Huang D, Ma N, Li X, Gou Y, Duan Y, Liu B, Xia J, Zhao X, Wang X, Li Q, Rao J, Zhang X. 2023. Advances in single-cell RNA sequencing and its applications in cancer research. *J Hematol Oncol* **16**:98. doi:10.1186/s13045-023-01494-6

Idrisova KF, Simon HU, Gomzikova MO. 2022. Role of Patient-Derived Models of Cancer in Translational Oncology. *Cancers (Basel)* **15**:139. doi: 10.3390/cancers15010139.

Jo JA, Cheng S, Cuenca-Martinez R, Duran-Sierra E, Malik B, Ahmed B, Maitland K, Cheng YL, Wright J, Reese T. 2018. Endogenous Fluorescence Lifetime Imaging (FLIM) Endoscopy For Early Detection Of Oral Cancer And Dysplasia. *Annu Int Conf IEEE Eng Med Biol Soc* **2018**:3009–3012. doi: 10.1109/EMBC.2018.8513027.

Kalinina S, Freymueller C, Naskar N, von Einem B, Reess K, Sroka R, Rueck A. 2021. Bioenergetic Alterations of Metabolic Redox Coenzymes as NADH, FAD and FMN by Means of Fluorescence Lifetime Imaging Techniques. *Int J Mol Sci* **22**:5952. doi:10.3390/ijms22115952.

Kim J, DeBerardinis RJ. 2019. Mechanisms and Implications of Metabolic Heterogeneity in Cancer. *Cell Metabolism* **30**:434–446. doi:10.1016/j.cmet.2019.08.013

Lagarto JL, Shcheslavskiy V, Pavone FS, Cicchi R. 2020. Real-time fiber-based fluorescence lifetime imaging with synchronous external illumination: A new path for clinical translationю *J Biophot* **13**:e201960119. doi: 10.1002/jbio.201960119.

Lakowicz JR, Szmacinski H, Nowaczyk K, Johnson ML. 1992. Fluorescence lifetime imaging of free and protein-bound NADH. *Proc Natl Acad Sci USA* **89**:1271–1275. doi: 10.1073/pnas.89.4.1271.

Lea T. 2015. Caco-2 Cell Line In: Verhoeckx K, Cotter P, López-Expósito I, Kleiveland C, Lea T, Mackie A, Requena T, Swiatecka D, Wichers H, editors. The Impact of Food Bioactives on Health. Cham: Springer International Publishing. pp. 103–111. doi:10.1007/978-3-319-16104-4_10

Lin D, Fan W, Zhang R, Zhao E, Li P, Zhou W, Peng J, Li L. 2021. Molecular subtype identification and prognosis stratification by a metabolism-related gene expression signature in colorectal cancer. *J Transl Med* **19**:279. doi:10.1186/s12967-021-02952-w

Liu X, Wang S-C, Ni M, Xie Q, Zhang Y-F, Lv W-F, Geng G-Y. 2022. Correlation between 18F-FDG PET/CT intra-tumor metabolic heterogeneity parameters and KRAS mutation in colorectal cancer. *Abdom Radiol* **47**:1255–1264. doi:10.1007/s00261-022-03432-5

Liu X, Xiang K, Geng G-Y, Wang S-C, Ni M, Zhang Y-F, Pan H-F, Lv W-F. 2022. Prognostic Value of Intratumor Metabolic Heterogeneity Parameters on 18F-FDG PET/CT for Patients with Colorectal Cancer. *Contrast Media & Molecular Imaging* **2022**:1–11. doi:10.1155/2022/2586245

Lukina MM, Dudenkova VV, Ignatova NI, Druzhkova IN, Shimolina LE, Zagaynova EV, Shirmanova MV. 2018. Metabolic cofactors NAD(P)H and FAD as potential indicators of cancer cell response to chemotherapy with paclitaxel. *Biochimica et Biophysica Acta (BBA) – General Subjects* **1862**:1693–1700. doi:10.1016/j.bbagen.2018.04.021

Lukina MM, Shimolina LE, Kiselev NM, Zagainov VE, Komarov DV, Zagaynova EV, Shirmanova MV. 2019. Interrogation of tumor metabolism in tissue samples *ex vivo* using fluorescence lifetime imaging of NAD(P)H. *Methods Appl Fluoresc* **8**:014002. doi:10.1088/2050-6120/ab4ed8

Marusyk A, Polyak K. 2010. Tumor heterogeneity: Causes and consequences. *Biochimica et Biophysica Acta (BBA) – Reviews on Cancer* **1805**:105–117. doi:10.1016/j.bbcan.2009.11.002

Masson N, Ratcliffe PJ. 2014. Hypoxia signaling pathways in cancer metabolism: the importance of co-selecting interconnected physiological pathways. *Cancer Metab* **2**:3. doi:10.1186/2049-3002-2-3

Mizuno Y, Hattori K, Taniguchi K, Tanaka K, Uchiyama K, Hirose Y. 2020. Intratumoral heterogeneity of glutaminase and lactate dehydrogenase A protein expression in colorectal cancer. *Oncol Lett* **19**:2934–2942. doi: 10.3892/ol.2020.11390.

Mycek MA, Schomacker KT, Nishioka NS. 1998. Colonic polyp differentiation using time-resolved autofluorescence spectroscopy. *Gastrointest Endosc* **48**:390–394. doi: 10.1016/s0016-5107(98)70009-4.

Offermans K, Jenniskens JC, Simons CC, Samarska I, Fazzi GE, Smits KM, Schouten LJ, Weijenberg MP, Grabsch HI, van den Brandt PA. 2022. Expression of proteins associated with the Warburg-effect and survival in colorectal cancer. *J Pathol Clin Res* **8**:169–180. doi: 10.1002/cjp2.250.

Parshina YP, Komarova AD, Bochkarev LN, Kovylina TA, Plekhanov AA, Klapshina LG, Konev AN, Mozherov AM, Shchechkin ID, Sirotkina MA, Shcheslavskiy VI, Shirmanova

MV. 2022. Simultaneous Probing of Metabolism and Oxygenation of Tumors In Vivo Using FLIM of NAD(P)H and PLIM of a New Polymeric Ir(III) Oxygen Sensor. *IJMS* **23**:10263. doi:10.3390/ijms231810263

Pavlova NN, Thompson CB. 2016. The Emerging Hallmarks of Cancer Metabolism. *Cell Metabolism* **23**:27–47. doi:10.1016/j.cmet.2015.12.006

Pinho DF, King B, Xi Y, Albuquerque K, Lea J, Subramaniam RM. 2020. Value of Intratumoral Metabolic Heterogeneity and Quantitative ^{18}F-FDG PET/CT Parameters in Predicting Prognosis for Patients With Cervical Cancer. *American Journal of Roentgenology* **214**:908–916. doi:10.2214/AJR.19.21604

Plathow C, Weber WA. 2008. Tumor Cell Metabolism Imaging. *J Nucl Med* **49**:43S-63S. doi:10.2967/jnumed.107.045930

Rück A, Hauser C, Mosch S, Kalinina S. 2014. Spectrally resolved fluorescence lifetime imaging to investigate cell metabolism in malignant and nonmalignant oral mucosa cells. *J Biomed Opt* **19**:96005. doi:10.1117/1.JBO.19.9.096005.

Seidenari S, Arginelli F, Bassoli S, Cautela J, French P, Guanti M, Guardoli D, König K, Talbot C, Dunsby C. 2012. Multiphoton Laser Microscopy and Fluorescence Lifetime Imaging for the Evaluation of the Skin. *Dermatology Research and Practice* **2012**:810749. https://doi.org/10.1155/2012/810749.

Sengupta D, Pratx G. 2016. Imaging metabolic heterogeneity in cancer. *Mol Cancer* **15**:4. doi:10.1186/s12943-015-0481-3

Seth Nanda C, Venkateswaran SV, Patani N, Yuneva M. 2020. Defining a metabolic landscape of tumours: genome meets metabolism. *Br J Cancer* **122**:136–149. doi:10.1038/s41416-019-0663-7

Shah AT, Diggins KE, Walsh AJ, Irish JM, Skala MC. 2015. In Vivo Autofluorescence Imaging of Tumor Heterogeneity in Response to Treatment. *Neoplasia* **17**:862–870. doi:10.1016/j.neo.2015.11.006

Shah AT, Heaster TM, Skala MC. 2017. Metabolic Imaging of Head and Neck Cancer Organoids. *PLoS ONE* **12**:e0170415. doi:10.1371/journal.pone.0170415

Sharick JT, Jeffery JJ, Karim MR, Walsh CM, Esbona K, Cook RS, Skala MC. 2019. Cellular Metabolic Heterogeneity In Vivo Is Recapitulated in Tumor Organoids. *Neoplasia* **21**:615–626. doi:10.1016/j.neo.2019.04.004

Sharick JT, Walsh CM, Sprackling CM, Pasch CA, Pham DL, Esbona K, Choudhary A, Garcia-Valera R, Burkard ME, McGregor SM, Matkowskyj KA, Parikh AA, Meszoely IM, Kelley MC, Tsai S, Deming DA, Skala MC. 2020. Metabolic Heterogeneity in Patient

Tumor-Derived Organoids by Primary Site and Drug Treatment. *Front Oncol* **10**:553. doi:10.3389/fonc.2020.00553

Shirmanova M, Sergeeva T, Druzhkova I, Meleshina A, Lukina M, Dudenkova V, Shcheslavskiy V, Becker W, Belousov V, Mishina N, Zagaynova E. 2018. Metabolic shifts in cell proliferation and differentiation In: König K, editor. Multiphoton Microscopy and Fluorescence Lifetime Imaging. De Gruyter. pp. 189–208. doi:10.1515/9783110429985-012

Shirmanova MV, Gorbachev DA, Sarkisyan KS, Parnes AP, Gavrina AI, Polozova AV, Kovaleva TF, Snopova LB, Dudenkova VV, Zagaynova EV, Lukyanov KA. 2021. FUCCI-Red: a single-color cell cycle indicator for fluorescence lifetime imaging. *Cell Mol Life Sci* **78**:3467–3476. doi:10.1007/s00018-020-03712-7

Shirmanova MV, Sinyushkina SD, Komarova AD. 2023. Metabolic Heterogeneity of Tumors. *Molecular Biology* **57**(6):1125–1142. doi:10.31857/S0026898423060186.

Shirshin EA, Shirmanova MV, Gayer AV, Lukina MM, Nikonova EE, Yakimov BP, Budylin GS, Dudenkova VV, Ignatova NI, Komarov DV, Yakovlev VV, Becker W, Zagaynova EV, Shcheslavskiy VI, Scully MO. 2022. Label-free sensing of cells with fluorescence lifetime imaging: The quest for metabolic heterogeneity. *Proc Natl Acad Sci USA* **119**:e2118241119. doi:10.1073/pnas.2118241119

Skala MC, Deming DA, Kratz JD. 2022. Technologies to Assess Drug Response and Heterogeneity in Patient-Derived Cancer Organoids. *Annu Rev Biomed Eng* **24**:157–177. doi:10.1146/annurev-bioeng-110220-123503

Smith JT, Yao R, Sinsuebphon N, Rudkouskaya A, Un N, Mazurkiewicz J, Barroso M, Yan P, Intes X. 2019. Fast fit-free analysis of fluorescence lifetime imaging via deep learning. *Proc Natl Acad Sci USA* **116**:24019–24030. doi: 10.1073/pnas.1912707116.

Stine ZE, Walton ZE, Altman BJ, Hsieh AL, Dang CV. 2015. MYC, Metabolism, and Cancer. *Cancer Discovery* **5**:1024–1039. doi:10.1158/2159-8290.CD-15-0507

Sun Y, Phipps JE, Meier J, Hatami N, Poirier B, Elson DS, Farwell DG, Marcu L. 2013. Endoscopic Fluorescence Lifetime Imaging for *In Vivo* Intraoperative Diagnosis of Oral Carcinoma. *Microsc Microanal* **19**:791–798. doi:10.1017/S1431927613001530

van der Laak J, Litjens G, Ciompi F. 2021. Deep learning in histopathology: the path to the clinic. *Nat Med* **27**:775–784. https://doi.org/10.1038/s41591-021-01343-4.

Varshavi Dorna, Varshavi Dorsa, McCarthy N, Veselkov K, Keun HC, Everett JR. 2020. Metabolic characterization of colorectal cancer cells harbouring different KRAS mutations in codon 12, 13, 61 and 146 using human SW48 isogenic cell lines. *Metabolomics* **16**:51. doi:10.1007/s11306-020-01674-2

Wallrabe H, Svindrych Z, Alam SR, Siller KH, Wang T, Kashatus D, Hu S, Periasamy A. 2018. Segmented cell analyses to measure redox states of autofluorescent NAD(P)H, FAD & Trp in cancer cells by FLIM. *Sci Rep* **8**:79. doi: 10.1038/s41598-017-18634-x.

Walsh AJ, Castellanos JA, Nagathihalli NS, Merchant NB, Skala MC. 2016. Optical Imaging of Drug-Induced Metabolism Changes in Murine and Human Pancreatic Cancer Organoids Reveals Heterogeneous Drug Response. *Pancreas* **45**:863–869. doi:10.1097/MPA.0000000000000543

Walsh AJ, Cook RS, Sanders ME, Aurisicchio L, Ciliberto G, Arteaga CL, Skala MC. 2014. Quantitative Optical Imaging of Primary Tumor Organoid Metabolism Predicts Drug Response in Breast Cancer. *Cancer Research* **74**:5184–5194. doi:10.1158/0008-5472.CAN-14-0663

Walsh AJ, Cook RS, Skala MC. 2017. Functional Optical Imaging of Primary Human Tumor Organoids: Development of a Personalized Drug Screen. *J Nucl Med* **58**:1367–1372. doi:10.2967/jnumed.117.192534

Wang J, Wen S, Symmans WF, Pusztai L, Coombes KR. 2009. The Bimodality Index: A criterion for Discovering and Ranking Bimodal Signatures from Cancer Gene Expression Profiling Data. *Cancer Inform* **7**:CIN.S2846. doi:10.4137/CIN.S2846

Weyers BW, Birkeland AC, Marsden MA, Tam A, Bec J, Frusciante RP, Gui D, Bewley AF, Abouyared M, Marcu L, Farwell DG. 2022. Intraoperative delineation of p16+ oropharyngeal carcinoma of unknown primary origin with fluorescence lifetime imaging: Preliminary report. *Head & neck* **44**:1765–1776. doi: 10.1002/hed.27078.

Yoshida GJ. 2015. Metabolic reprogramming: the emerging concept and associated therapeutic strategies. *J Exp Clin Cancer Res* **34**:111. doi:10.1186/s13046-015-0221-y

Yuzhakova D, Kiseleva E, Shirmanova M, Shcheslavskiy V, Sachkova D, Snopova L, Bederina E, Lukina M, Dudenkova V, Yusubalieva G, Belovezhets T, Matvienko D, Baklaushev V. 2022. Highly Invasive Fluorescent/Bioluminescent Patient-Derived Orthotopic Model of Glioblastoma in Mice. *Front Oncol* **12**:897839. doi:10.3389/fonc.2022.897839

Yuzhakova DV, Lukina MM, Sachkova DA, Yusubalieva GM, Baklaushev VP, Mozherov AM, Dudenkova VV, Gavrina AI, Yashin KS, Shirmanova MV. 2023. Development of a 3D Tumor Spheroid Model from the Patient's Glioblastoma Cells and Its Study by Metabolic Fluorescence Lifetime Imaging. *Sovrem Tehnol Med* **15**:28. doi:10.17691/stm2023.15.2.03

Zhang L, Liu Y, Ding Y, Deng Y, Chen H, Hu F, Fan J, Lan X, Cao W. 2023. Predictive value of intratumoral-metabolic heterogeneity derived from 18F-FDG PET/CT in distinguishing microsatellite instability status of colorectal carcinoma. *Front Oncol* **13**:1065744. doi:10.3389/fonc.2023.1065744

Zhang M, Wang H, Peng R, Xu F, Wang F, Zhao Q. 2020. Metabolism-Associated Molecular Classification of Colorectal Cancer. *Front Oncol* **10**:602498. doi:10.3389/fonc.2020.602498

Zhou D, Duan Z, Li Z, Ge F, Wei R, Kong L. 2022. The significance of glycolysis in tumor progression and its relationship with the tumor microenvironment. *Front Pharmacol* **13**:1091779. doi:10.3389/fphar.2022.1091779

Author information

Anastasia D Komarova

Institute of Experimental Oncology and Biomedical Technologies, Privolzhsky Research Medical University, Nizhny Novgorod, Russia; Institute of Biology and Biomedicine, Lobachevsky State University of Nizhny Novgorod, Nizhny Novgorod, Russia

Contribution: investigation, visualization, writing—original draft

Contributed equally with: Snezhana D Sinyushkina and Ilia D Shchechkin

Competing interests: No competing interests declared

Snezhana D Sinyushkina

Institute of Experimental Oncology and Biomedical Technologies, Privolzhsky Research Medical University, Nizhny Novgorod, Russia

Contribution: investigation, visualization, writing—original draft

Contributed equally with: Anastasia D Komarova and Ilia D Shchechkin

Competing interests: No competing interests declared

Ilia D Shchechkin

Institute of Experimental Oncology and Biomedical Technologies, Privolzhsky Research Medical University, Nizhny Novgorod, Russia; Institute of Biology and Biomedicine, Lobachevsky State University of Nizhny Novgorod, Nizhny Novgorod, Russia

Contribution: investigation, visualization, writing—original draft

Contributed equally with: Anastasia D Komarova and Snezhana D Sinyushkina

Competing interests: No competing interests declared

Irina N Druzhkova

Institute of Experimental Oncology and Biomedical Technologies, Privolzhsky Research Medical University, Nizhny Novgorod, Russia

Contribution: funding acquisition, investigation, visualization

Competing interests: No competing interests declared

Sofia A Smirnova

Institute of Experimental Oncology and Biomedical Technologies, Privolzhsky Research Medical University, Nizhny Novgorod, Russia

Contribution: investigation

Competing interests: No competing interests declared

Vitaliy M Terekhov

Nizhny Novgorod Regional Oncologic Hospital, Nizhny Novgorod, Russia

Contribution: investigation

Competing interests: No competing interests declared

Artem M Mozherov

Institute of Experimental Oncology and Biomedical Technologies, Privolzhsky Research Medical University, Nizhny Novgorod, Russia

Contribution: investigation

Competing interests: No competing interests declared

Nadezhda I Ignatova

Institute of Experimental Oncology and Biomedical Technologies, Privolzhsky Research Medical University, Nizhny Novgorod, Russia

Contribution: investigation

Competing interests: No competing interests declared

Elena E Nikonova

Laboratory of Clinical Biophotonics, Sechenov First Moscow State Medical University, Moscow, Russia

Contribution: methodology

Competing interests: No competing interests declared

Evgeny A Shirshin

Laboratory of Clinical Biophotonics, Sechenov First Moscow State Medical University, Moscow, Russia; Faculty of Physics, Lomonosov Moscow State University, Moscow, Russia

Contribution: data curation, methodology, writing—review and editing

Competing interests: No competing interests declared

Liubov E Shimolina

Institute of Experimental Oncology and Biomedical Technologies, Privolzhsky Research Medical University, Nizhny Novgorod, Russia

Contribution: investigation

Competing interests: No competing interests declared

Sergey V Gamayunov

Nizhny Novgorod Regional Oncologic Hospital, Nizhny Novgorod, Russia

Contribution: investigation, data curation, validation

Competing interests: No competing interests declared

Vladislav I Shcheslavskiy

Institute of Experimental Oncology and Biomedical Technologies, Privolzhsky Research Medical University, Nizhny Novgorod, Russia; Becker&Hickl GmbH, Germany

Contribution: data curation, validation, writing—review and editing

Competing interests: No competing interests declared

Marina V Shirmanova

Institute of Experimental Oncology and Biomedical Technologies, Privolzhsky Research Medical University, Nizhny Novgorod, Russia

Contribution: conceptualization, data curation, project administration, supervision, writing—original draft, writing—review and editing

For correspondence: Shirmanovam@mail.ru

Competing interests: No competing interests declared

Supplementary

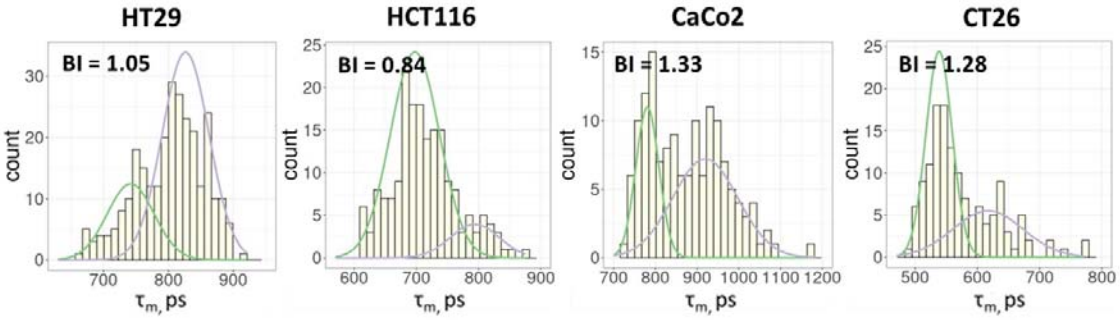

Figure S1. FLIM of NAD(P)H in monolayer cell cultures. The distribution of the NAD(P)H-τ_m for the cell lines. The bimodality index (BI-τ_m) is shown on each diagram.

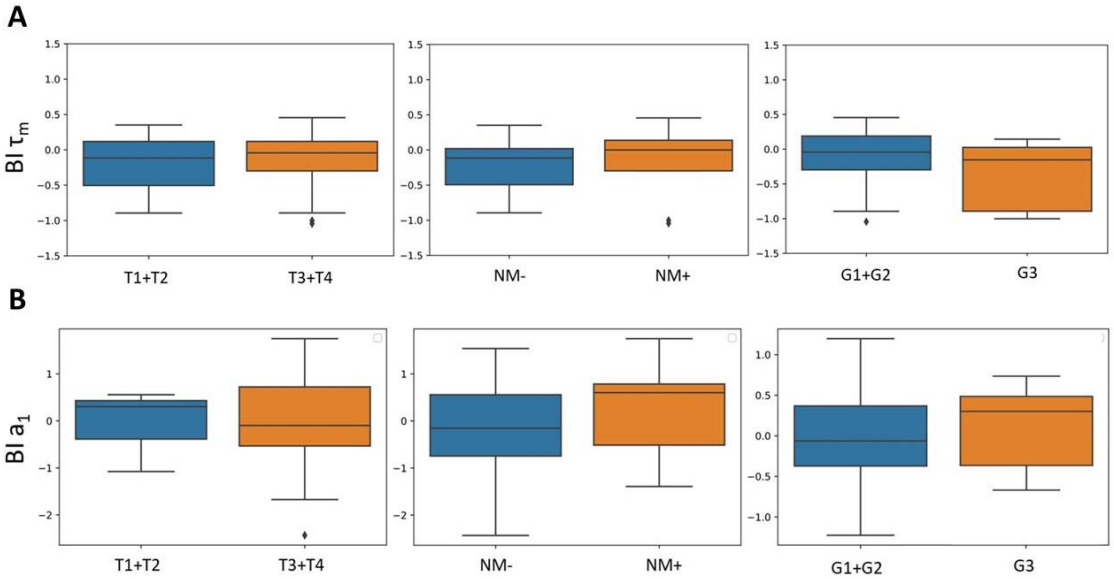

Figure S2. The relationships between parameters BI-τ_m (A) and BI-a_1 (B) and clinicopathological characteristics of patients' tumors. No significant differences were found between the groups.

Immunohistochemical analysis of EpCAM and vimentin

Tissue sections were stained with primary antibodies to epithelial cell adhesion molecule EpCAM (ThermoFisher Scientific, mouse, cat. #14-9326-82, dilution 1:700) and an intermediate filament protein vimentin (Abcam, ab137321, rabbit, dilution 1:700), according to the manufacturer's protocol. Secondary antibodies goat anti-mouse (Alexa Fluor 488) and goat anti-rabbit (Alexa Fluor 555) were used. Tissue sections were imaged using EVOS

M7000 Imaging System (Thermo Fisher Scientific Inc., Waltham, MA USA) with LED cubes GFP (ex.470/22 nm, em.510/42 nm for Alexa 488) and RFP (ex.531/40 nm, em. 593/40 nm for Alexa 555) at x20 magnification.

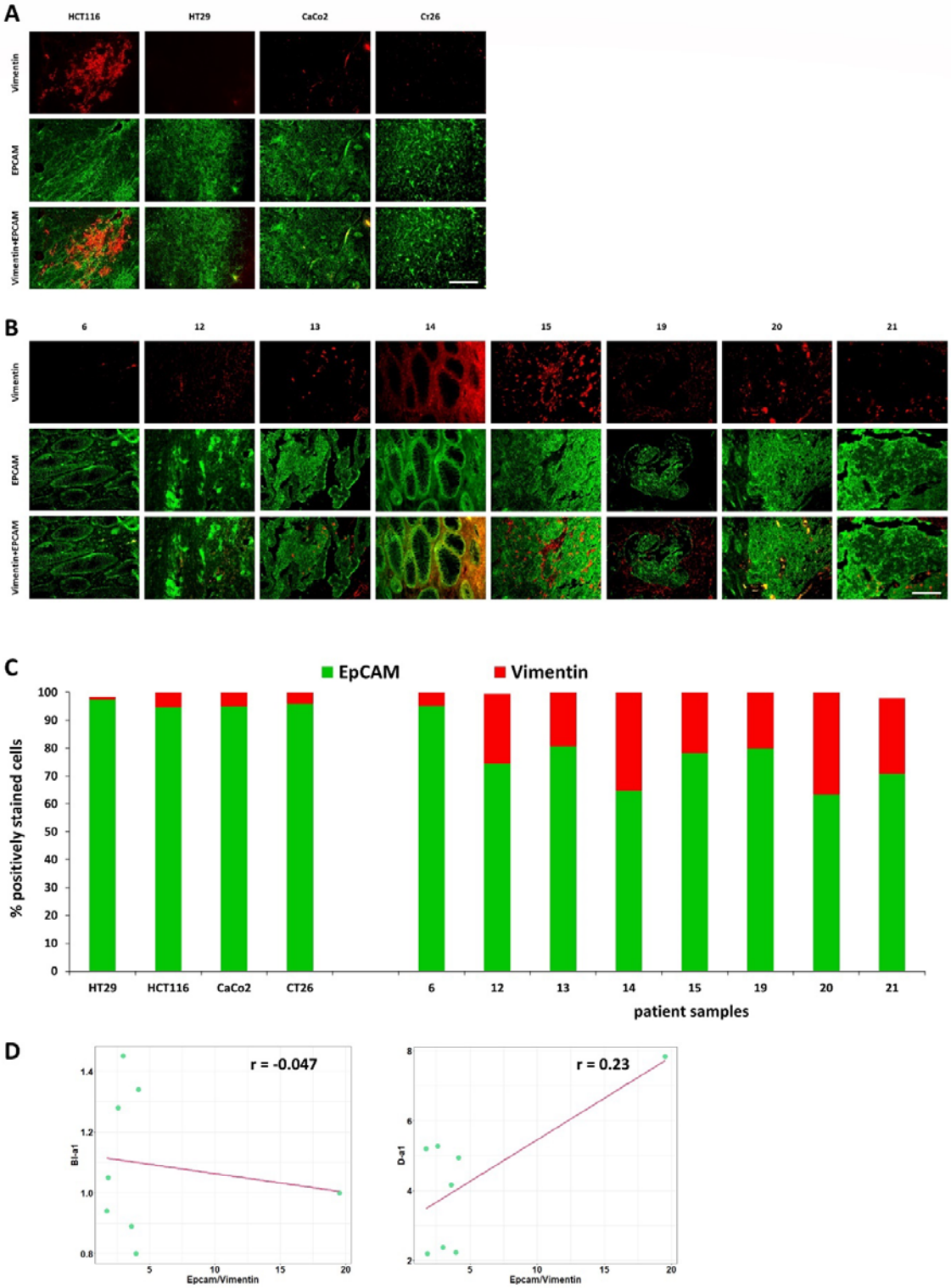

Figure S3. Immunohistochemical analysis of the expression of EpCAM (green, epithelial cells marker) and vimentin (red, mesenchymal cells marker) in tumors. (**A**) Immunofluorescence images of HT29, HCT116, CaCo2 and CT26 mouse tumors. Scale bar = 100 μm. (**B**) Immunofluorescence images of patients' tumors (numbered from 6 to 21). Scale bar = 100 μm. (**C**) The ratio of EpCAM-positive to vimentin-positive areas in tumor sections. (**D**) The bimodality index (BI-a_1) and dispersion (D-a_1) plotted against the EpCAM/vimentin ratio in patient tumor samples. Pearson correlation r is shown on the plots.

Immunohistochemical analysis of LDHA and GLUT3 expression

Immunohistochemical staining was performed using immunostainer «Bond-Max» (Leica Biosistems, UK) with BOND 5.1 software, according to the standard protocols recommended by the manufacturer. Staining protocol included preliminary dewaxing of the sections and unmasking in a high pH buffer based on ethylenediaminetetraacetic acid for 20 minutes at 98-99°C. Next, slides were incubated with primary polyclonal antibodies to Glucose Transporter 3 GLUT3 (E-AB-31557, Elabscience, China) or to Lactate dehydrogenase A LDHA (E-AB-19947, Elabscience, China) for 15 minutes. For the antibodies detection «Bond polymer refine detection system» (Leica Biosystems, UK) was used. To create an electronic archive of the received material, the digital automatic scanner 3DHISTECH PANNORAMIC Midi (Carl Zeiss, Germany) was used. The images were obtained at magnifications 5x, 10x, 20x, 40x, 63x, resolution 0.087 μm/pixel. The staining intensity was visually evaluated as negative (-) low (+), moderate (++) or high (+++).

Due to the expression of GLUT3 and LDHA in all cell types and, especially, in cancer cells the 100% of cells within the samples had positive staining. The diffuse cytoplasmic staining with weak granularity was observed. Five out of seven tumor samples stained for LDHA had a high (+++) expression level and other two - moderate (++). GLUT3 expression level varied from the low (+) to the high (+++).

One can see from representative IHC images that the expression level of glycolytic enzymes provides some information about intertumor metabolic differences, but is insensitive to intercellular variability of metabolism registered by NAD(P)H FLIM.

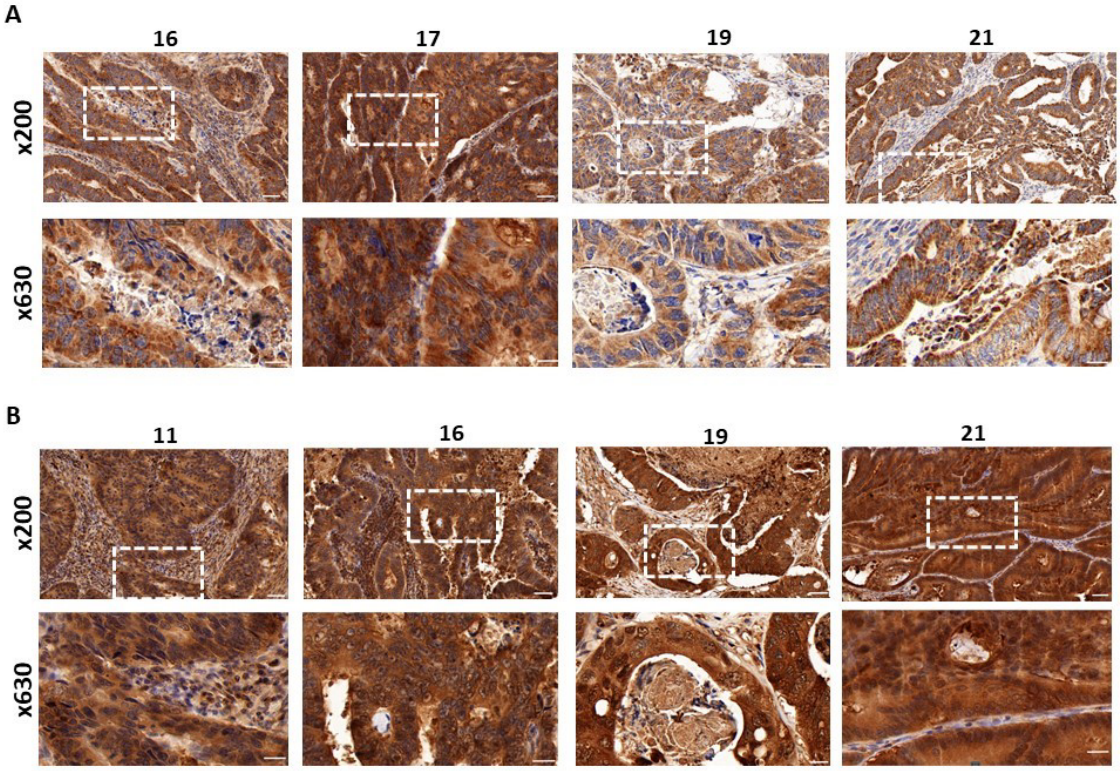

C

The immunoexpression level

patient №	11	12	15	16	17	19	20	21
LDHA	++	+++	++	+++		+++	+++	+++
GLUT3				++	+++	+		+

Figure S4. Immunohistochemical analysis of the expression of GLUT3 and LDHA in patients' tumors. (**A**) Representative immunohistochemical images of GLUT3 expression. Scale bar = 50 μm (magnification x200) and 20 μm (magnification x630). (**B**) Representative immunohistochemical images of LDHA expression. Scale bar = 50 μm (magnification x200) and 20 μm (magnification x630). (**C**) Semi-quantitative evaluation of the expression level by staining intensity.

Fluorescence of flavins in colorectal cancer

Fig.S5 shows the examples of fluorescence intensity images of flavins (FAD) and NAD(P)H in patients' samples of colorectal cancer. Flavins fluorescence was excited at a wavelength of 900 nm and detected in the range of 500–550 nm, average laser power applied to the samples was ~6 mW. The fluorescence intensity of flavins in colorectal cancer cells (in vitro, in vivo and ex vivo) was very low, comparable with background signal. The average number of photons per pixel recorded was only 78 for flavins and 2145 photons for

NAD(P)H. For bi-exponential fitting, at least 5000 photons per the curve are required for reliable fluorescence lifetime evaluation. Such a photon budget is not available for flavins even with a pixel binning in a single cell level. Therefore, analysis of the fluorescence lifetime of FAD in colorectal cancer samples was impossible.

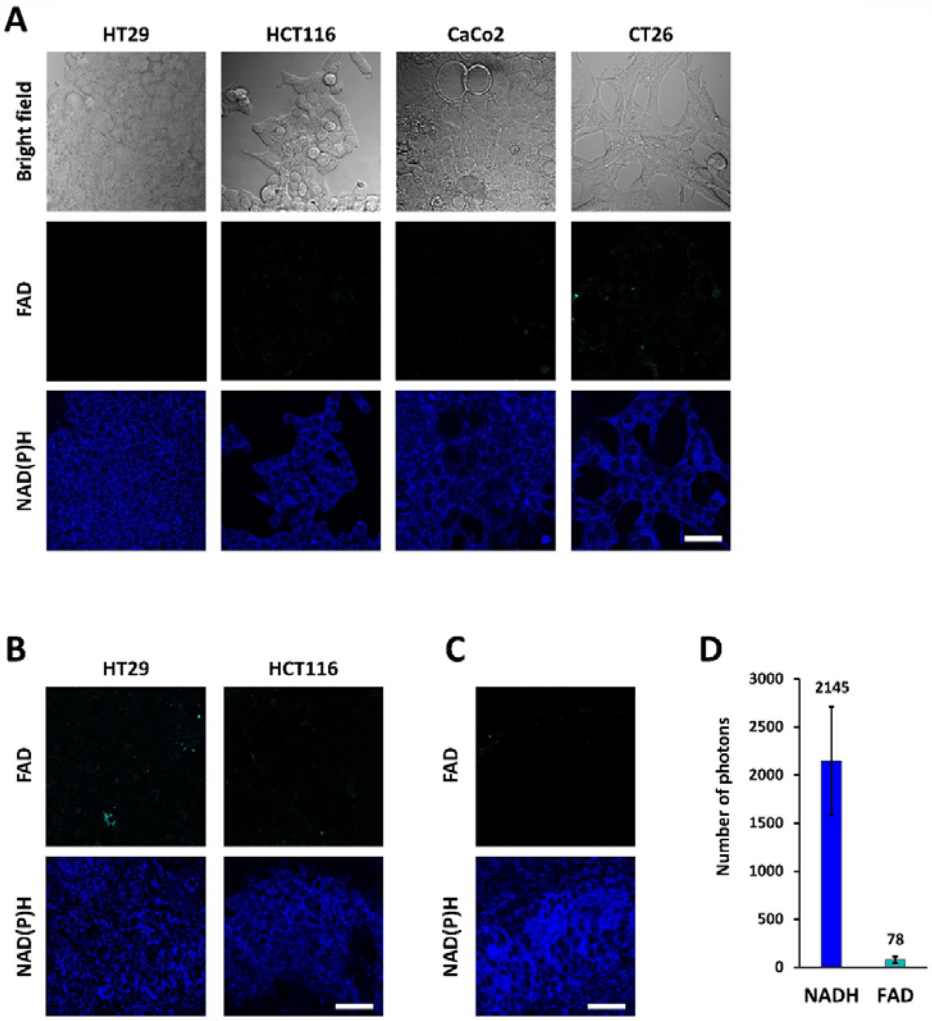

Figure S5. Autofluorescence of cofactors FAD and NAD(P)H. Representative fluorescence intensity images of FAD (ex. 900 nm, em. 500–550 nm) and NAD(P)H (ex. 750 nm, em. 450–490 nm) in cultured cells **(A)**, tumor xenografts in vivo **(B)** and patient tumor ex vivo (№ 11) **(C).** Scale bar = 50 μm. **D** – The number of photons per pixel recorded by FLIM for flavins in ex vivo patient samples. Mean±SD, n=7 patients.

Table S1. NAD(P)H fluorescence decay parameters of colorectal cancer cells in monolayer cultures in vitro and in mouse tumors in vivo.

τ_m – mean lifetime, τ_1 – short lifetime component, τ_2 – long lifetime component, a_1 – relative contribution of the short lifetime component, BI-τ_m – bimodality index of the mean lifetime.

Cell line	τ_m, ns	τ_1, ns	τ_2, ns	a_1, %	BI-τ_m
Cell lines in vitro					
HT29	0.80±0.05	0.39±0.03	2.47±0.17	80.11±1.34	1.05
HCT116	0.71±0.05	0.40±0.02	2.39±0.20	84.13±1.58	0.84
CaCo2	0.95±0.10	0.38±0,05	2.53±0.24	73.48±2.26	1.19
CT26	0.57±0.06	0.35±0.03	2.03±0.22	86.48±1.28	1.28
Tumors in vivo					
HT29	0.85[0.81;0.90]	0.46[0.45;0.48]	2.70[2.59;2.79]	82.68[80.79;83.65]	1.13±0.37
HCT116	0.88[0.85;0.92]	0.47[0.45;0.48]	2.67[2.56;2.77]	80.61[79.32;81.96]	0.91±0.28
CaCo2	1.03[0.92;1.10]	0.44[0.40;0.47]	2.98[2.75;3.12]	76.46[75.07;78.42]	1.41±0.61
CT26	0.73[0.69;0.78]	0.39[0.37;0.41]	2.38[2.22;2.53]	82.77[81.05;84.20]	1.12±0.37

Table S2. Clinicopathological characteristics of patients' tumors.

№	Tumor site	Tumor type	Tumor stage	Tumor grade
1	Rectum colon	Adenocarcinoma	cT4bN1M0 (stage IIIB)	High
2	Sigmoid colon	Serrated Adenocarcinoma	T4aN0M0 (stage IIB)	Moderate
3	Transverse colon	Adenocarcinoma	T4bN0M0 (stage IIB)	High
4	Sigmoid colon	Serrated Adenocarcinoma	T1N0M0 (stage I)	Low
5	Sigmoid colon	Serrated Adenocarcinoma	pT3N0M0 (stage IIA)	Moderate
6	Sigmoid colon	Adenoma-like Adenocarcinoma	pT3bN0M0 (stage IIA)	Moderate
7	Hepatic flexure	Poorly Cohesive Adenocarcinoma	pT4aN0M1c (stage IV)	High
8	Rectum colon	Adenoma-like Adenocarcinoma	pT2N0M0 (stage I)	Moderate
9	Sigmoid colon	Adenocarcinoma	pR0T3N2bM0 (stage IIIC)	High
10	Rectum colon	Adenoma-like Adenocarcinoma	pT2N0M0 (stage I)	Low
11	Sigmoid colon	Adenocarcinoma	T3N1M0 (stage IIIB)	Moderate
12	Transverse colon	Adenocarcinoma	T3N0M1 (stage IV)	Moderate

13	Cecum colon	Adenocarcinoma	T3N1M0 (stage IIIB)	Moderate
14	Rectum colon	Adenocarcinoma	T3N1M0 (stage IIIB)	Moderate
15	Cecum colon	Adenocarcinoma	T3N1M0 (stage IIIB)	Low
16	Rectum colon	Adenocarcinoma	T3N1M0 (stage IIIB)	Moderate
17	Hepatic flexure	Adenocarcinoma	T3N0pM1c (stage IV)	Moderate
18	Transverse colon	Adenocarcinoma	T3N0M1c (stage IV)	High
19	Sigmoid colon	Adenocarcinoma	cT4bN1M0c (stage IIIB)	Moderate
20	Sigmoid colon	Adenocarcinoma	T3N0M0 (stage IIA)	Moderate
21	Transverse colon	Adenocarcinoma	cT3N1M0 (stage IIIB)	Low
22	Transverse colon	Adenocarcinoma	T4N2M1 (stage IV)	Moderate
23	Transverse colon	Adenocarcinoma	T3N1M0 (stage IIIB)	Moderate
24	Rectum colon	Adenocarcinoma	T3N0M0 (stage IIA)	Moderate
25	Transverse colon	Adenocarcinoma	pT3N1aM0 (stage IIIB)	High-grade
26	Transverse colon	Adenocarcinoma	T4N0M0 (stage IIB)	Moderate
27	Hepatic flexure	Adenocarcinoma	pT3N1bM0 (stage IIIB)	Moderate
28	Hepatic flexure	Adenocarcinoma	cT3N0M0 (stage IIA)	Moderate
29	Transverse colon	Adenocarcinoma	T4N0M0 (stage IIA)	Moderate

Table S3. NAD(P)H fluorescence decay parameters of patients' tumors ex vivo.

№	τ_m, ns	τ_1, ns	τ_2, ns	a_1, %	BI-τ_m
1	1.21[1.08;1.31]	0.50[0.44;0.55]	2.68[2.26;3.01]	67.30[62.74;70.61]	1.15
2	1.03[0.97;1.08]	0.50[0.47;0.52]	2.89[2.65;3.04]	76.92[74.76;79.05]	1.04
3	1.05[0.98;1.12]	0.46[0.42;0.52]	1.99[1.79;2.31]	61.96[57.17;66.07]	0.29
4	0.90[0.83;0.97]	0.41[0.38;0.46]	1.83[1.64;2.15]	64.79[60.15;72.47]	0.93
5	1.00[0.94;1.08]	0.46[0.43;0.50]	2.14[1.85;2.38]	67.88[63.63;70.69]	0.62
6	1.03[0.96;1.11]	0.50[0.46;0.53]	2.06[1.81;2.29]	64.99[61.13;68.97]	0.88
7	1.01[0.92;1.07]	0.45[0.39;0.49]	1.91[1.76;2.14]	62.84[58.47;67.94]	1.05
8	0.98[0.90;1.09]	0.44[0.41;0.49]	2.28[1.99;2.58]	70.85[66.26;74.53]	0.29
9	0.86[0.78;0.95]	0.35[0.30;0.39]	2.12[1.76;2.58]	72.20[66.23;77.82]	0.20
10	0.88[0.84;0.98]	0.45[0.42;0.50]	2.31[2.07;2.57]	76.33[72.32;79.41]	1.32
11	1.14[1.04;1.23]	0.49[0.46;0.51]	3.00[2.82;3.18]	74.06[71.47;76.07]	1.08
12	1.20[1.13;1.26]	0.50[0.49;0.52]	2.96[2.82;3.13]	71.08[70.29;72.93]	1.40

13	1.19[1.16;1.23]	0.51[0.42;0.53]	2.98[2.80;3.16]	71.50[68.85;74.09]	1.14
14	1.00[9.70;1.04]	0.47[0.46;0.47]	2.86[2.80;2.95]	77.68[76.47;78.72]	0.78
15	1.30[1.23;1.38]	0.53[0.50;0.57]	3.09[2.86;3.37]	69.49[67.19;71.52]	0.78
16	0.87[0.79;0.97]	0.44[0.41;0.47]	2.67[2.51;2.82]	80.24[78.45;81.91]	0.98
17	1.05[0.94;1.19]	0.43[0.36;0.47]	3.10[2.83;3.21]	74.45[72.21;78.50]	1.00
18	1.23[1.18;1.29]	0.50[0.48;0.52]	3.00[2.87;3.22]	70.76[68.03;73.49]	0.90
19	0.93[0.90;0.97]	0.47[0.44;0.48]	2.75[2.60;2.87]	79.21[77.71;80.05]	1.31
20	0.81[0.74;1.41]	0.23[0.21;0.55]	2.33[2.16;3.23]	70.63[68.41;73.97]	4.24
21	1.13[1.01;1.20]	0.49[0.48;0.52]	3.22[3.03;3.31]	77.22[73.68;79.47]	0.17
22	1.11[0.94;1.24]	0.47[0.34;0.46]	2.72[2.42; 3.05]	76.37[74.95;78.24]	1.07
23	1.17[0.99;1.39]	0.51[0.41;0.56]	2.84[2.23;3.52]	76.08[72.41;78.95]	1.91
24	1.12[0.99;1.19]	0.37[0.31;0.41]	2.56[2.32;2.86]	77.17[73.77;79.54]	1.34
25	0.94[0.76;1.08]	0.48[0.42;0.52]	2.64[2.35;2.89]	79.75[77.12;81.99]	1.32
26	1.29[1.18;1.36]	0.47[0.43;0.52]	3.08[2.88;3.43]	78.92[75.34;81.17]	0.66
27	1.06[1.01;1.12]	0.48[0.42;0.54]	2.44[2.32;2.62]	74.06[72.86;77.01]	0.66
28	1.31[1.18;1.51]	0.50[0.47;0.53]	3.13[2.78;3.58]	78.25[75.33;81.01]	1.4
29	1.03[0.92;1.21]	0.48[0.46;0.52]	2.38[2.07;2.85]	76.65[73.44;79.82]	0.86

Table S4. Statistical significance of the differences of NAD(P)H a_1-% between different cell lines and tumors (p-values).

Cell lines in vitro			
	HT29	HCT116	CaCo2
HCT116	$8.56 \cdot 10^{-108}$	-	-
CaCo2	$1.58 \cdot 10^{-71}$	$1.72 \cdot 10^{-83}$	-
CT26	$2.53 \cdot 10^{-166}$	$2.09 \cdot 10^{-36}$	$2.45 \cdot 10^{-92}$
Tumors in vivo			
	HT29	HCT116	CaCo2
HCT116	0.1	-	-
CaCo2	0.057	0.057	-
CT26	0.727	0.064	0.0028